ICTP – EC COST Action ES0803 – EC FP7 Project SOTERIA - INAF – ESA
International Advanced School on Space Weather Modelling and Applications

Lecture Notes on

Ground-based Instrumentation for Space Weather Observations in Geospace.

Peter Stauning
Danish Meteorological Institute
pst@dmi.dk

Table of contents.

1. Introduction. The Carrington event.
2. Geospace
  2.2. The Earth's magnetic field
  2.3. The Earth's upper atmosphere and ionosphere
3. Magnetic measurements, current systems and indices.
  3.1 Instrumentation.
  3.2. Current systems in Geospace
  3.3. Magnetic indices and data.
4. Ionospheric radiowave propagation
  4.1. Refraction
  4.2 Absorption
  4.3. Scatter and scintillations
5. Instrumentation for Ionospheric observations.
  5.1. Ionosonde
  5.2. Digisonde
  5.3. GPS TEC
  5.4. Riometer
  5.5. Coherent scatter radars
6. Concluding remarks.

1. Introduction. The Largest Magnetic Storm on Record: The Carrington Event.

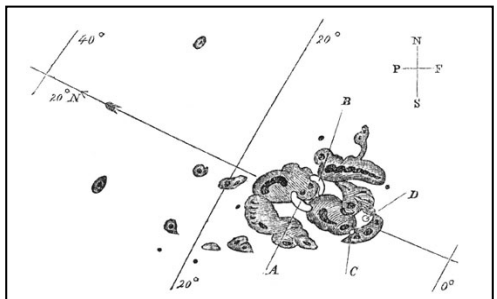

Figure 1.1. Carrington's sunspot drawing

1.1 Carrington's report to The Royal Astronomical Society:

Description of a Singular Appearance seen in the Sun on September 1, 1859. By R. C. Carrington, Esq.

"*While engaged in the forenoon of Thursday, Sept. 1, in taking my customary observation of the forms and positions of the solar spots, an appearance was witnessed which I believe to be exceedingly rare. The image of the sun's disk was, as usual with me, projected to a plate of glass coated with distemper. I had secured diagrams of all the groups and detached spots, when within the area of the great north group, two patches of intensely bright and white light broke out, in the positions indicated in the diagram by the letters A and B, and of the forms of spaces left white. I thereupon noted down the time by the chronometer, and seeing the outburst to be very rapidly on the increase, and being somewhat flurried by the surprise, I hastily ran to call some one to witness the exhibition with me, and on returning within 60 seconds, was mortified to find that it was already much changed and enfeebled. Very shortly afterwards the last trace was gone. The magnetic instruments at Kew were simultaneously disturbed to a great extent." (*Nov. 11, 1859)

The 'Carrington Event' Magnetic storm recorded at Greenwich Observatory, London

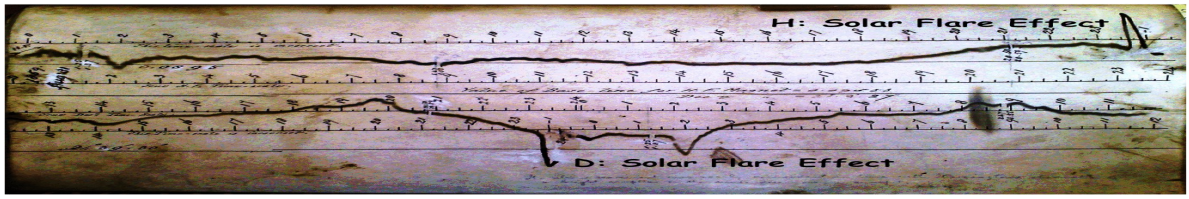

Figure 1.2a. SID onset 1 September 1859 11:15 UT ↑ Solar flare effect in D. Solar flare effect in H ↑

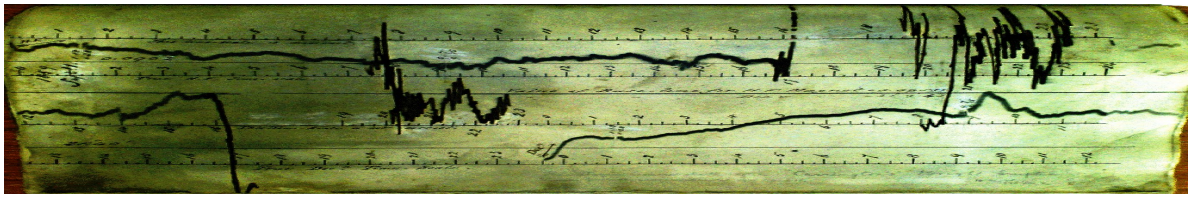

Figure 1.2b. ↑ Mag. storm effect in D. Mag. storm in H ↑ at 04:50 UT on 2 September 1859.

Declination, or compass direction, (D) is the lower trace on each image and the horizontal force (H) is the upper trace. Universal Time is the time recorded here (astronomical) plus 12 hours and measured D precedes H by approximately 12 hours. For reference the marked 'solar flare effect', beginning at 23:15 recorded astronomical time on August 31st, is at 11:15 Universal Time on September 1st. It has been measured as 110 nT in H and 0.283 degrees in D.

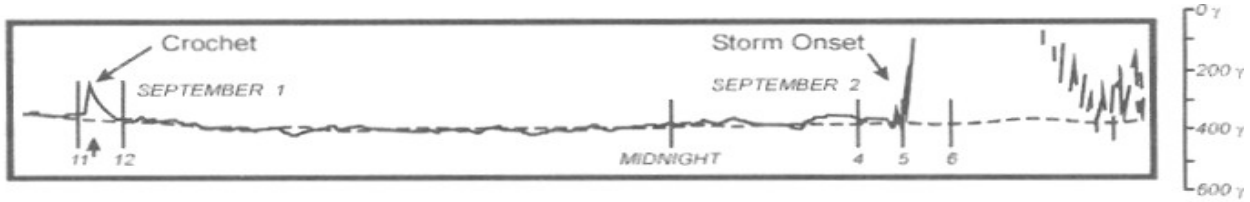

Figure 1.2c. Reconstruction of the course of the horizontal component during the Carrington event. (Bartels, 1937).

It should be noted that the Sun-Earth transit time was only 17.6 hours for this storm in contrast to the usual 2-4 days for moderate solar outbursts. Thus, the transit time from monitor satellites at the L1 Lagrange point, e.g., ACE, to the Earth would only be 11 minutes in this case, which is probably quite representative for the extremely violent storm cases. Note also the Storm Sudden Commencement (SSC) spike at "5" in Fig.1.2c.

1.2. Comparisons of more recent events to Carrington event

Lord Carrington was the first ever to witness and report a solar flare. Actually, another astronomer, R. Hodgeson (1860), also observed the flare. Carrington was aware of the simultaneous magnetic disturbances, but it was not until almost 80 years later that Julius Bartels (1937) made the connection between the Sudden Ionospheric Disturbance (SID) giving a "Crochet-like" magnetic disturbance and the onset of the succeeding magnetic storm following the arrival at the Earth of the intense solar wind enhancement resulting from the ejection of immense solar coronal masses (a CME).

The violent geomagnetic storm in the beginning of September 1859 caused numerous disturbances all over the world. Telegraph lines were disrupted, equipment were disabled and even destroyed by fires resulting from large induced voltages. Beautiful auroras occurred in unusual places closer to equator than ever seen before. It is now generally recognized that the Carrington event was exceptionally large. Thus it may serve to provide "worst case" benchmarks for possible Space Weather effects that could arrive in the future, if we could realistically scale its various effects. Extensive efforts have been made in this direction. An excellent review has been given by Cliver and Svalgaard (2004).

Typically, a solar eruption comprise three main features.
(i) **Solar flare**, which from the Earth is seen as an explosion-like bright flash accompanied by intense electromagnetic radiation at wavelengths stretching from X-ray and hard UV emissions to bursts at radio wave frequencies. In the sunlit upper atmosphere, the X-ray and UV emissions generate enhanced ionization, which in turn may cause enhanced ionospheric currents and absorption of radio waves.
(ii) **High-energy particle radiation**, notably protons, electrons, which may arrive at the Earth within 10-15 min. The solar protons can have energies in excess of 100 Mev. The charged particles are guided by the Earths magnetic field to enter the upper atmosphere over the polar caps where they generate enhanced ionization, which in turn cause radio wave absorption, Polar Cap Absorption (PCA). Some of the protons may interact with atmospheric atoms to form high-energy neutrons detectable at ground causing Ground Level Event (GLE).
(iii) **Coronal mass ejection (CME)**, where a cloud of hot coronal gas may be launched from the Sun forming a CME event. If ejected toward the Earth, the cloud may reach Geospace in 2-4 days and will generate geomagnetic storms and substorms during several days upon the arrival.

We may describe the terrestrial effects of a solar outburst event by the magnitude of various parameters:
(i) The amplitude of the Solar Flare Effect/Sudden Ionospheric Disturbance (SFE/SID) event.
(ii) The intensity of high-energy solar particle radiation.
(iii) The magnitude of the geomagnetic storm scaled by transit time and peak intensity.
(iv) The intensity of substorms scaled by the auroral electrojet currents and the latitudinal extent of auroras.

Within each category we can compare the magnitude of the Carrington storm with other solar-terrestrial disturbances observed later in order to rank the events and obtain a realistic impression of the possible "worst case" effects based on known consequences of recent similar occurrences.

(i) **Amplitudes of major SID events.**
The Magnetic Crochet or Solar Flare Effect (SFE) is seen in Figs. 1a. and 1c. above. Table 1 indicates that the amplitude of the SFE initiating the 1859 Carrington event was among the largest ever reported. It had a magnitude corresponding closely to the 28 October 2003 and 4 November 2003 events, which rank among the largest recorded solar eruptions. (Cliver and Svalgaard, 2004).

TABLE I

Outstanding solar flare effects at mid-latitudes identified in a literature search for events from 1936–1968 and from associations with > X10 soft X-ray flares, 1984–2003.

Date	1–8 Å Class	Magnetometer station	Zenith angle (°)	SFE amplitude (nT)
04 Nov. 2003	X28	Newport	63	115
28 Feb. 1942	–	Eskdalemuir	63	112
28 Oct. 2003	>X17	Tamanrasset	36	111
01 Sep. 1859	–	Greenwich	44	110
15 Jun. 1991	>X12	Hyderabad	22	95
06 Jun. 1991	>X12	Guam	20	90
15 Apr. 2001	>X15	Tamanrasset	34	85

(ii) **Intensities of major solar proton events.**
Figure 1.3. (after McCracken et al., 2001) presents a chronological display of all major events of >30 MeV solar proton fluences occurring during 1855-2001. Values prior to 1950 are based on analyses of ice core nitrate isotope composition. After 1950 the values are based on ionospheric measurements (e.g. riometer) and direct satellite measurements. A short list of the largest events arranged according to measured or inferred magnitude is displayed in Table 2 (from Cliver and Svalgaard, 2004). The Carrington event had a magnitude around twice that of the second largest events in the list and ~ four times that of the 4 August 1972 event or the 14 July 2000 "Bastille event", which both had ample satellite data coverage.

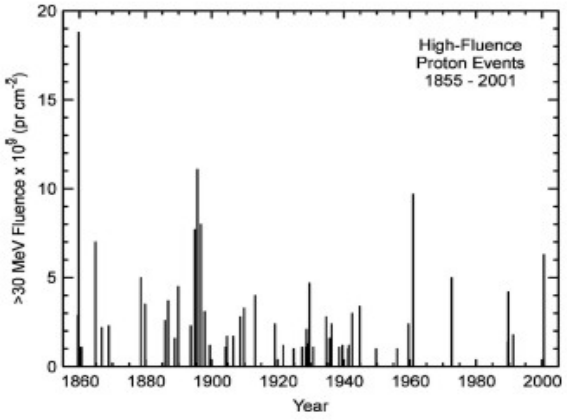

Figure 1.3. High-fluence >40 MeV solar proton events.

TABLE II
Large solar energetic proton events, 1859–2000[a].

Date[b]	>30 MeV SEP fluence (10^9 pr cm^{-2})
Aug.–Sep. 1859	18.8
1895	11.1
Nov. 1960	9.7
1896	8.0
1894	7.7
1864	7.0
Jul. 2000	6.3
1878	5.0
Aug. 1972	~5

(iii) **CME transit time.**
The Sun-Earth transit time is an important parameter for monitoring and warning of violent space weather events associated with solar CME outbursts. Usually, the transit time is related to the magnitude of the event such that the major events tend to have shorter transit times. Most CME's have average velocities between 400 and 800 km/s corresponding to transit times on the order of 2-4 days. However, the largest events tend to have transit times below 1 day corresponding to velocities around 2000 km/s.

Table III from Cliver and Svalgaard (2004) illustrates the transit times for some of the major events. For the largest CME events the transit time from solar wind monitors like the ACE satellite at the L1 Sun-Earth liberation point (240 Re~1,500,000 km) to the Earth is only 10-15 min in contrast to transit times around 1 hour for moderate CME events. Thus, for many practical applications, ground-based monitors would detect violent storm conditions almost as fast as the L1 monitor satellites.

TABLE III
"Fast-transit" events, 1859–2003.

Flare date	Transit time (h)
04 Aug. 1972	14.6
01 Sep. 1859	17.6
06 Feb. 1946	17.8
28 Feb. 1941	18.4
16 Jul. 1959	19.4
28 Feb. 1942	19.5
17 Sep. 1941	19.8
29 Oct. 2003	~20[a]
28 Oct. 2003	20.3[a]
15 Apr. 1938	21.2
12 Nov. 1960	21.2
16 Jan. 1938	21.8

(iv) **Peak magnitude of magnetic storms**.
One of the parameters to characterize the terrestrial effects of solar outbursts is the peak value of the magnetic variations recorded during the geomagnetic storm. Table IV from Cliver and Svalgaard (2004) presents the peak magnetic deflection for a number of great magnetic storms.

For the Carrington event, the magnetic measurements went off-scale except for the Z-component. Tsurutani et al. (2003) have estimated the peak excursion in the horizontal component at low-latitude stations to be ~1600 nT, which would put the Carrington event on top of the list presented in Table IV.

TABLE IV
Chronological listing of outstanding geomagnetic storms recorded at Greenwich/Abinger, 1859–1954[a].

	Ranges		
Date	Declination (′)	Horizontal force (nT)	Vertical (nT)
01 Sep. 1859	≫92	≫625	1500
04 Feb. 1872	125	800	>950
17 Nov. 1882	115	>1090	>1060
31 Oct. 1903	119	1175	1440
25 Sep. 1909	193	1710	>1080
14 May 1921	110	≫740	≫460
25 Jan. 1938[b]	126	1055	570
16 Apr. 1938	307	1375	500
24 Mar. 1940	131	1370	1000
01 Mar. 1941	186	1650	1310
18 Sep. 1941	123	1250	1115
28 Mar. 1946	162	1660	920
21 Sep. 1946	136	925	450

(v) **Latitudinal extent of auroras.**
The brilliant auroras are mostly the result of substorm activity. However, the latitudinal extent of the auroras can be linked to the magnitude of the geomagnetic storm. The reported observations of auroras in the North-American sector during the September 1859 Carrington storm are shown by the red spots in the map in Fig. 1.4. Table VII from Cliver and Svalgaard (2004) presents the equatormost latitude for auroral observations during this and some further major magnetic storm events.

TABLE VII
Low-latitude auroras, 1859–1958[a].

Date	Low-latitude extent	Reference
4 Feb. 1872[b]	19°	Chapman (1957a,b)
2 Sep. 1859	20°	Loomis (1859, 1860a,b, 1861); Kimball (1960)
11 Feb. 1958	28°	Adem (1958)
14 May. 1921	30° (see text)	Silverman and Cliver (2001)
25 Sep. 1909	30°	Silverman (1995)
25 Jan. 1938	30°	S. Silverman (personal communication, 2004)

Figure 1.4. Reported observations of auroras during the 1859 Carrington storm. (from: The Scientific American).

Conclusions on the relative magnitude of the Carrington storm.
In their analysis of the Carrington storm, Cliver and Svalgaard (2004) conclude that the effects of the September 1859 storm were not markedly larger (if larger at all) than those of the top tens of subsequent great storms, contrary to the findings of Tsurutani et al. (2003). However, at the same time, the 1859 space weather event stands alone as the single event that appears at or close to the top of all of the effect lists. Still, after 150 years, the first identified space weather event continues to be the largest ever recorded – across the activity spectrum.

References:
The Great Historical Geomagnetic Storm of 1859: A Modern Look, ed.: C. R. Clauer, Special Issue of Advances in Space Research, Vol. 38, No. 2., 2006.
Cliver, E. W., and L. Svalgaard (2004), The 1859 solar-terrestrial disturbance and the current limit of extreme space weather activity, Solar Phys. 224, 407-422,.

2. Geospace properties.

2.1. The Earth's magnetic field.

Around 97% of the main field is generated by electrical currents in the conducting core of fluid metal inside the non-conducting and non-magnetic mantle made of viscous minerals at temperatures above the Curie temperature (500-600°), where the minerals loose their magnetic properties. About 2-3% of the main field at the surface of the Earth is generated by magnetic minerals in the crust of thickness around 10-50 km down to the Curie temperature level. Fig. 2.1.1 illustrates the inner regions of the Earth and sketches the magnetic field lines.

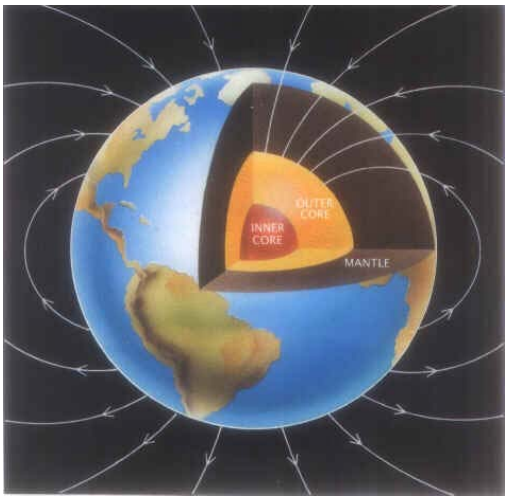

Figure 2.1.1. Earth's structure and magnetic field.

The electrical currents results from self-sustained generator effects in the convective motions within the highly conductive and rotating fluid core. Modelling the variable magnetic fields down to the core-mantle boundary makes it possible to construct an image of the fluid motion in the outermost reaches of the core. These vortex-like convection patterns are sketched in Fig. 2.1.2

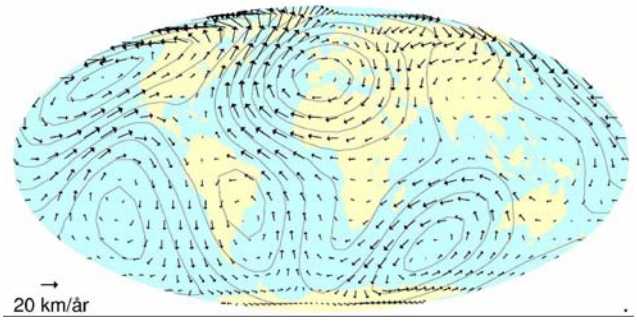

Figure 2.1.2. Convection patterns at the Core-Mantle Boundary.

Basically, the Earth's magnetic main field resembles the field from a dipole with magnetic moment M=7.788 x 10^{22} Am^2 (DGRF2000) mounted in the middle of the Earth. The dipole axis is inclined approximately 10.46 degrees with respect to the Earth's rotational axis. The northern pole (magnetic south pole) is positioned at (79.54°, 288.43°). The dipole magnetic moment is decreasing at around 1% per decade and the position of the axial poles varies. At present the northern pole is moving toward the geographic pole.

The vertical (radial) component, Z, and the horizontal component, H, of dipole magnetic field can be derived from the magnetic potential V, which in turn is calculated from the magnetic moment M by:

$$V=\frac{\mathbf{M}\cdot\mathbf{r}}{r^3}=-\frac{M\sin\Phi}{r^2} \qquad Z=\frac{\partial V}{\partial r}=\frac{2M\sin\Phi}{r^3} \qquad H=\frac{\partial V}{r\partial\Phi}=\frac{M\cos\Phi}{r^3} \qquad (2.1.1)$$

where Φ is the latitude with respect to the magnetic equator.

A better approximation to the real field may be obtained by the eccentric dipole model where the assumed dipole is displaced from the centre of the Earth by around 540 km but keep the axis orientation and the magnetic moment. In a (X, Y, Z) coordinate system where the Z-axis is the Earth's rotational axis while the X-axis points to the Greenwich meridian, the eccentric dipole was located at (-401.86 km, 300.25 km, 200.61 km) in year 2000. For the eccentric dipole the northern and southern axial pole positions were (83.03°, 266.70°) and (-75.34°, 118.66°), respectively. The centred and eccentric dipole axial positions should not be confused with the dip pole positions where the actual magnetic field is vertical. In 2000 the northern and southern dip poles were located at (82.66°, -168.60°) and (-66.06°, 128.04°), respectively.

The representation of the geomagnetic field by the centred or the eccentric dipole field is adequate for many space weather applications. For more demanding applications a more precise modelling might be required. The mathematical formulation of the presently used model of the Earths magnetic field was developed by the German Professor C. F. Gauss around 1830. The model expresses the magnetic potential, V, through an expansion using spherical harmonics functions. The field components are calculated from the derivatives of the potential similar to the expressions in Eq. 2.1.1. However, now the field also depends on azimuth.

$$
\begin{aligned}
V = a \Bigg\{ & \sum_{n=1}^{19} \sum_{m=0}^{n} \left(g_n^m \cos m\phi + h_n^m \sin m\phi\right) \left(\frac{a}{r}\right)^{n+1} P_n^m(\cos\theta) \\
& + \sum_{n=1}^{2} \sum_{m=0}^{n} \left(q_n^m \cos m\phi + s_n^m \sin m\phi\right) \left(\frac{r}{a}\right)^{n} P_n^m(\cos\theta) \\
& + Dst \cdot \left[\left(\frac{r}{a}\right) + Q_1 \left(\frac{a}{r}\right)^2 \right] \cdot \\
& \left[\tilde{q}_1^0 P_1^0(\cos\theta) + \left(\tilde{q}_1^1 \cos\phi + \tilde{s}_1^1 \sin\phi\right) P_1^1(\cos\theta) \right] \Bigg\} .
\end{aligned}
\qquad (2.1.2.)
$$

Here, Earth's radius is a, r is the geocentric distance, θ is the geographic co-latitude, while φ is the geographical longitude. P_n^m are normalized spherical harmonics functions. The coefficients g_n^m, h_n^m ,q_n^m , and s_n^m are found by approximating the model to real field values measured from observatories at ground and from satellites (e.g. Magsat, Oersted, and CHAMP). They vary with time and are usually tabulated along with their time derivatives.

In contrast to the slowly varying main field contribution from internal sources, the external current systems in the ionosphere and magnetosphere generate additional contributions on the order of 1-5% varying at speeds ranging from few seconds to several days. The magnitude of the most regular of these external currents can be characterized by indices, for instance the ring current index Dst, and included in the modelling of the total field as shown in the last part of the formula in Eq.2.1.2.

Tabulations of the most recent field models may be found at various magnetic data centres. A much used version is the International Geomagnetic Reference Field Model (IGRF) derived every 5 years and in time updated to become Definitive Geomagnetic Reference Field models (DGRF). A graphical representation of the global field magnitude is shown in Fig. 2.1.3. Note the two northern high-intensity regions, one over northern Canada, the other over Siberia. The southern hemisphere has only one polar high-intensity field region. Note also the deep minimum, the so-called South Atlantic Anomaly, in the South America-South Atlantic region.

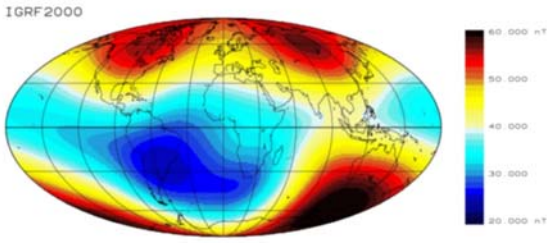

Figure 2.1.3. Representation of surface magnetic field strength based on IGRF 2000. **(**Stauning, 2004)

Links and further reading:

General information on IGRF: http://nssdc.gsfc.nasa.gov/space/model/magnetos/igrf.html
Tables of coefficients and programs to calculate field components: http://ccmc.gsfc.nasa.gov/modelweb/
NOAA/IAGA IGRF web site: http://www.ngdc.noaa.gov/IAGA/vmod/igrf.html
Some web sites includes a calculator service to provide on-line calculations of the main field based on the IGRF model for any specified location upon input of its geographical coordinates:
British Geological Survey: http://www.geomag.bgs.ac.uk/gifs/igrf_form.shtml
Canadian Natural Resources webservice: http://gsc.nrcan.gc.ca/geomag/data/index_e.php

Reference book: J. A. Jacobs (editor): Geomagnetism. Vol. 1-4. Academic Press Ltd. 1987-1991.

2.2. The Earth's upper atmosphere and ionosphere.

In a simplified model the atmosphere and ionosphere in the height range from 50 to 500 km could be subdivided in various regions as sketched in Fig. 2.2.1. In the right field the atmosphere is subdivided in regions according to the characteristic process that dominate the composition within the region. The regions below around 100 km have a composition much like the lowermost part (Troposphere) of the atmosphere. Further up the composition is gradually changed to comprise more helium and hydrogen molecules and atoms. In the middle field the atmosphere is subdivided according to temperature. In the left field the ionosphere is subdivided in D, E, F (F1, F2) layers, for which typical electron density profiles are shown for daytime and nighttime conditions, respectively.

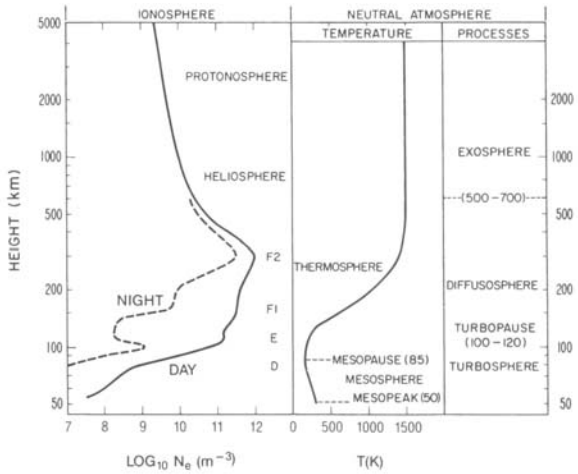

Figure 2.2.1. Atmosphere and ionosphere characteristics (after VanZandt and Knecht, 1964. In: Davies, 2008, p.57)

The neutral atmosphere. The atmospheric pressure, p, and density, ρ, at temperature T and height h are defined by the barometric equations:

$$p = p_0 \exp\left(-\int_{h_0}^{h} \frac{dh}{H_p}\right) \qquad (2.2.1)$$

$$\rho T = \rho_0 T_0 \exp\left(-\int_{h_0}^{h} \frac{dh}{H_p}\right) \qquad (2.2.2)$$

where p_0 is the pressure, ρ_0 the density, and T_0 the temperature at the reference height h_0. H_p is the pressure (neutral) scale height defined by:

$$H_p = \frac{KT}{\bar{m}g} \qquad (2.2.3)$$

depending on gravity, g, and on the mean molecular mass, m, at the altitude.
In and isothermal atmosphere the pressure and density profiles are given by:

$$p = p_0 \exp\left(-\frac{h - h_0}{H}\right) \qquad (2.2.4)$$

$$\rho = \rho_0 \exp\left(-\frac{h - h_0}{H}\right) \qquad (2.2.5)$$

In a perfect gas, where p=NKT and ρ=Nm, the scale height in km is given at any altitude by:

$$H = 0{\cdot}85\left(1 + \frac{h}{a}\right)^2 \frac{T}{M} \qquad (2.2.6)$$

where M is the molecular mass in grammols at height h, while a is the radius of the Earth (6372 km). At ground level, where M~29, T~300°K, the scale height is H~8 km.

Below ~120 km the temperature profile has a complicated structure with local minima at the tropopause and at the mesopause. Above 120 km the temperature increases asymptotically to reach the exospheric temperature level, T_∞ , which varies with latitude and local time depending on the intensity of solar UV flux and the geomagnetic activity (e.g., CIRA 1972, MSIS).

The Ionosphere. For a simplified case with a single solar wavelength that ionizes a one-component isothermal gas, the rate of ion production is given by the Chapman function:

$$q(z, \chi) = q_0 \exp [1 - z - \sec \chi \exp (-z)] \quad (2.2.7)$$

where z is the normalized height related to the pressure scale height H_p through:

$$z = (h - h_0)/H_p \quad (2.2.8)$$

while χ is the solar zenith angle and q_0 the ion production rate at level z=0 (i.e., $h=h_0$) and overhead sun (i.e., $\chi=0$) defined by:

$$q_0 = \phi(\infty)\eta/H_p\varepsilon \quad (2.2.9)$$

Here φ_∞ is the solar UV flux at the top of the atmosphere, η is the ionization efficiency (ion pairs each photon), and ε=2.718.

For other than overhead conditions (i.e., $\chi\neq0$) the height, z_m (or h_m), of maximum ion production rate, q_m, are given by:

$$z_m = \ln \sec \chi \quad (2.2.10a)$$
$$h_m = h_0 + H_p \ln \sec \chi \quad (2.2.10b)$$
$$q_m = q_0 \cos \chi \quad (2.2.10c)$$

The temporal changes in the electron density are controlled by the ion production rate q and the recombination rate coefficient α through the continuity equation:

$$\frac{dN_e}{dt} = q - \alpha N_e^2 \quad (2.2.11)$$

In equilibrium (i.e., $dN_e/dt=0$) the electron density profile is defined by:

$$N_e = N_{e0} \exp \tfrac{1}{2} [1 - z - \sec \chi \exp (-z)] \quad (2.2.12)$$

and the maximum electron density N_m at height h_m is given by:

$$N_m(\chi) = N_{e0} \cos^{1/2} \chi \quad (2.2.13)$$

where $N_{e0}=(q_0/\alpha)^{1/2}$ is the maximum electron density at overhead Sun.
The scale height for the ionized medium with ion and electron temperatures T_i and T_e is given by:

$$H_{pl} = \frac{K(T_e + T_i)}{gM_i} \quad (2.2.14)$$

where the electron mass has been neglected compared to the much greater ion mass M_i. In thermal equilibrium (i.e., $T_i=T_e$) the equation reduces to:

$$H_{pl} = \frac{2KT}{M_i g} \qquad (2.2.15)$$

These equations define the electron-ion density profile for a so-called Chapman layer. In a coarse model for quiet conditions the ionosphere could be considered to be the result of the superposition of three Chapman-like layers, namely the D, E, and F1 layers, and an additional uppermost layer, the F2 layer. In the F2 layer the recombination rate is very low and the electron-ion content is determined by a combination of vertical drift and diffusion processes and horizontal drift from and to the surrounding regions. The horizontal drift of ionization is affected both by the drift of the neutral constituents and by possible large-scale electric fields. An example of calculated thermospheric neutral winds over the northern hemisphere at 300 km altitude is displayed in Fig.2.2.2.

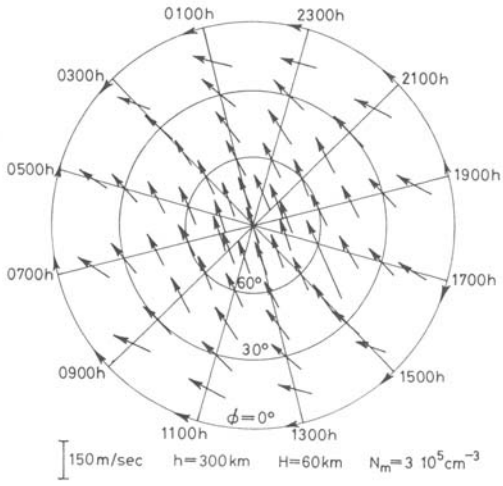

Figure 2.2.2. Polar view of thermospheric winds. From Kohl and King, 1967. In: Davies, 2008, p. 67)

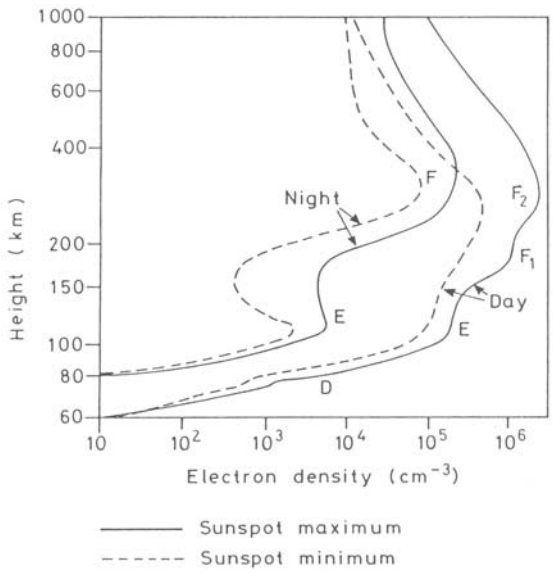

Figure 2.2.3. Electron density profiles at day/night and sunspot max/min. (From Hargreaves, 1992, p.209)

In the quiet D-region the dominant source process is photoionization of nitric oxide (NO) by Lyman-α UV radiation. During solar flares the enhancements of hard X-rays in the range from 1 to 10 Å may also ionize the D-region. In the E-region, the ionization of molecular oxygen (O_2) by UV radiation in the range from 912 to 1027 Å is important. During strong solar activity, soft X-rays in the range from 8 to 140 Å may contribute significantly. For the F1 region the ionization of atomic oxygen (O) by solar radiation within the wavelength range between 140 and 911 Å is particularly important.

Although exceedingly simple considering the vast number of lines in the solar spectrum and the large number of different molecular and atomic species in the upper atmosphere, the model explains many of the features of the real ionosphere like the regular daily and seasonal variations in electron densities and layer heights and the dependencies on the varying solar and geomagnetic activities through the solar cycle illustrated in Fig. 2.2.3.

Comprehensive quantitative modelling of the ionosphere is provided by the International Reference Ionosphere (IRI) model, available at http://ccmc.gsfc.nasa.gov/modelweb/

Electron and ion motions. In an ionized medium like the ionosphere the individual ions and electrons are no longer attached to each other but move in the applied electric and magnetic fields according to the fundamental "microscopic" equation of motion:

$$m\, d\mathbf{v}/dt = q\,(\mathbf{E} + \mathbf{v} \times \mathbf{B}) - m\,\mathbf{v}\,\nu \qquad (2.2.15)$$

where m and q are the mass and charge of the charged particle, **v** its velocity, **E** and **B** the electric and magnetic fields, while ν is the "effective" collision frequency at which the particle loos all its ordered

momentum by colliding with another charged or neutral particle. Without a magnetic field the particles would move in the direction of the electric field until stopped by collisions. In a magnetic field the **v** x **B** force is perpendicular to the motion and causes the charged particles to move in circles around the field direction. In combined electric and magnetic fields the motion of the charged particles can often be described as a gyration around the magnetic field combined with longitudinal and transverse drift.

The microscopic equation of motion is useful, among other, to describe the motion of individual high-energy charged particles in the Earth's environment (e.g. radiation belts) or to describe the collective electron motion (e.g., in wave fields). In a collision-dominated plasma (like the ionosphere), and for some applications the ionized medium is best treated as a "gas" of electrons and ions at temperatures T_e and T_i (which need not be equal) subjected to pressure forces in addition to the electric and magnetic forces. Assuming a Maxwell-Boltzmann distribution of the velocities for each of the plasma components, the thermal motion of the charged particles can be described by an effective temperature, T, by setting the average kinetic energy, ½ mv^2 equal to 3/2 KT, where K is the Boltzmann's constant ($1.381\ 10^{-23}$ joule/Kelvin). Thus the average root mean square (rms) velocity, v_{rms}, is :

$$v_{rms} = (3KT/m)^{½} \qquad (2.2.16)$$

Due to the strong electric field arising from excess charges, the medium will effectively maintain charge neutrality in any volume down to dimensions corresponding to the Debye length, $\lambda_D = (\varepsilon_0\, KT_e/q^2N_e)^{½}$, which for the ionosphere is typically 1-10 mm.

Conductivities. In order to derive the currents from the electric fields, the ionospheric conductivities are required. For the electric field and current components in a plane perpendicular to the magnetic field the conductivities in the direction of the electric field and transverse to the field, respectively, are:

$$\sigma_1 = \left[\frac{N_e}{m_e\nu_e}\left(\frac{\nu_e^2}{\nu_e^2+\omega_e^2}\right) + \frac{N_i}{m_i\nu_i}\left(\frac{\nu_i^2}{\nu_i^2+\omega_i^2}\right)\right]|e|^2 \qquad (2.2.17)$$

$$\sigma_2 = \left[\frac{N_e}{m_e\nu_e}\left(\frac{\omega_e\nu_e}{\nu_e^2+\omega_e^2}\right) - \frac{N_i}{m_i\nu_i}\left(\frac{\omega_i\nu_i}{\nu_i^2+\omega_i^2}\right)\right]|e|^2 \qquad (2.2.18)$$

while the conductivity that applies to the components of the electric fields and currents in the direction of the magnetic field is:

$$\sigma_0 = \left[\frac{N_e}{m_e\nu_e} + \frac{N_i}{m_i\nu_i}\right]|e|^2 \qquad (2.2.19)$$

In these expressions for a specific ionospheric region, N_e and N_i are the electron and ion densities, ν_e and ν_i are the collision frequencies, ω_e and ω_i are gyrofrequencies ($\omega_{e,i} = eB/ m_{e,i}$). The constants, m_e and m_i , are electron and ion masses, while |e| is the electron charge. The conductivity component σ_1 is called the Pedersen conductivity while σ_2 is the Hall conductivity. For many applications, the quantities of interest for the ionospheric electrodynamics are the vertically integrated Pedersen and Hall conductivities, Σ_P and Σ_H.

Links and further reading

Atmospheric models:
Coordinated Community Modelling Center: http://ccmc.gsfc.nasa.gov/modelweb/
Exospheric H Model: http://nssdc.gsfc.nasa.gov/space/model/atmos/h_exos.html

Ionospheric models:
Introduction to the Ionosphere: http://www.swpc.noaa.gov/info/Iono.pdf
General info on ionospheric models: http://nssdc.gsfc.nasa.gov/space/model/ionos/about_ionos.html
Global assimilative ionosphere model (GAIM): http://iono.jpl.nasa.gov/gaim/intro.html

Reference books:
Brekke, A. (1997), Physics of the Upper Polar Atmosphere, John Wiley & Sons.
Davies, K. (1990, 2008), Ionospheric Radio, First Edition: 1990, Peregrinus Ltd., Reprinted: 2008, The Institution of Engineering and Technology, London.
Hargreaves, J. K. (1992), The Solar-Terrestrial Environment, Cambridge University Press.
Kohl, H., R. Rüster, and K. Schlegel (eds.), Modern Ionospheric Science, European Geophysical Society, FRG 1996.

3. Magnetic measurements, current systems and indices.

3.1. Magnetic instrumentation.

Earlier, most magnetic instruments were based on using a suspended magnet either as a pendulum or as a compass-needle. The pendulum version developed by Gauss to provide an absolute measurement of the total horizontal component is displayed in Fig. 3.3.1. The magnet is suspended in a silk fibre and is free to oscillate in the horizontal plane. The magnet has at its end a small mirror by which the reflection of the length scale can be observed through the telescope. Weights can be added at the transverse bar to increase the moment of inertia. The Earths magnetic field provides a torque, **L,** proportional to the cross-product of the magnetic moment of the magnet, **M**, and the strength of the ambient magnetic field, **H**, i.e., **L** = **M** x **H**. For small deflections the torque is proportional to the deflection and the period of oscillations is given by $T=2\pi(K/MH)^{1/2}$ where K is the moment of inertia. The instrument can also be used as declinometer (compass needle) to measure variations in the declination of the magnetic field when the oscillations have died out.

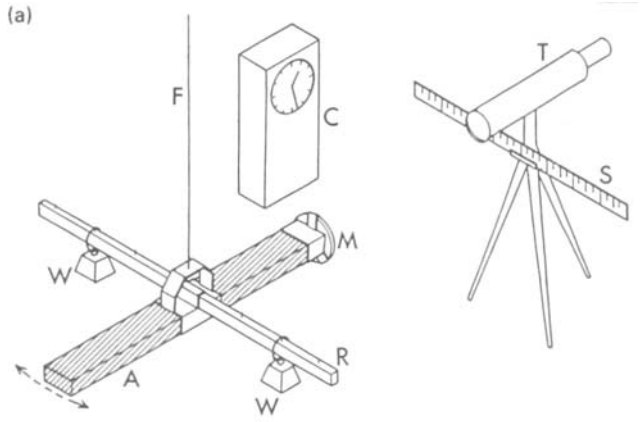

Figure 3.1.1. Gauss pendulum magnetometer. [Malin (1987), in Jacobs vol.1, p.15]

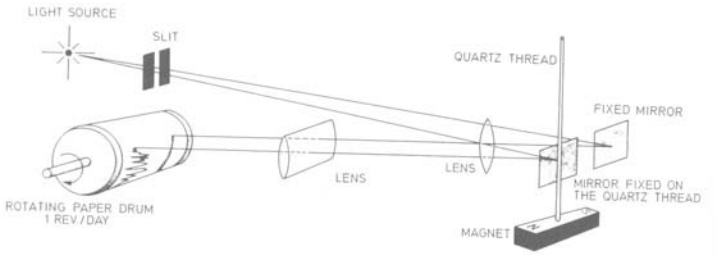

Figure 3.1.2. Torsion magnetograph. Principles of a Quarts Horizontal Magnetometer (QHM). [Brekke (1997), p.136]

A development to provide recordings of the magnetic variations is illustrated in Fig. 3.1.2. The light beam is reflected from the mirror attached to the suspended magnet and focused to produce a spot on the photographic paper mounted at the rotating drum. The reflections of the beam by a fixed mirror produce a reference level. The suspension could either be a silk fibre (as in Fig. 3.1.1) for recording of the declination or a quarts fibre to produce a torque. The mount of the quartz fibre (not shown) is rotated such that there is an initial torque in fibre opposite of that produced by the ambient magnetic field. Thus the resulting deflection provides a measure of the horizontal magnetic field strength.

Modern magnetic observatories most often use a combination of flux-gate magnetometers to provide individual measurements of the magnetic components and nuclear resonance magnetometers to provide absolute measurements of the magnetic field strength. The flux-gate principles are illustrated in Fig. 3.1.3. The cores a and b are made from high permeability magnetic material and have windings to carry the excitation current. The sinusoidal excitation current drives the cores into deep saturation in the positive as well as in the negative half period as illustrated in the B-H diagram.

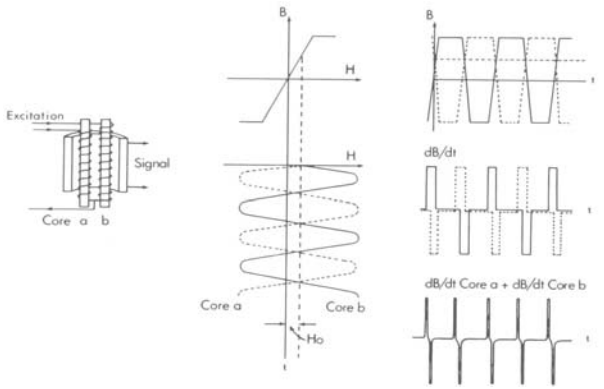

Figure 3.1.3. Principles of fluxgate sensors. [Forbes (1987), in Jacobs, vol.1, p.109]

A secondary coil picks up the induced signal produced by the flux change N dΦ/dt = N·A·dB/dt , where N is the number of turns on the secondary coil while Φ=A·B is the total magnetic flux through the area, A, of the secondary coil. The flux changes only during the short intervals where the coils are not saturated. Thus the contribution from each core will produce alternating short pulses. If there were no external field then the contributions from the two cores would be equal in magnitude and would cancel each other to provide a "null-signal". With an external field along the axis the two sets of pulses are shifted oppositely in phase such that the resulting induced signal will grow with the strength of the field. In most applications a bias current is fed to the secondary coil in order to produce a magnetic field that cancels the external field whereby the null-signal is obtained. Figure 3.1.4 illustrates the principles used for a practical flux-gate magnetometer. The rectified DC signal from the phase-sensitive detector (PSD) is amplified and used both to neutralize the magnetic field in the fluxgate sensor and to provide an output voltage for recording of the magnetic field variations around the adjustable bias level.

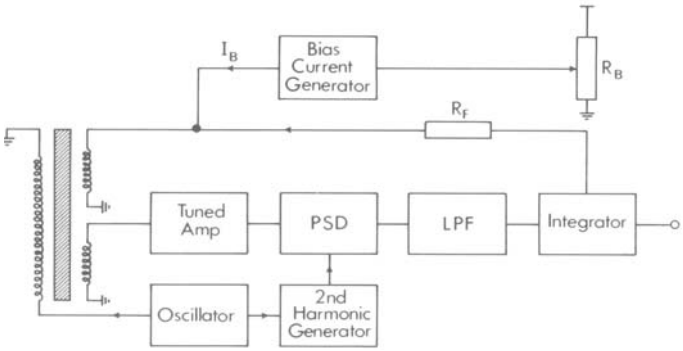

Figure 3.1.4. Fluxgate magnetometer principles. [Forbes (1987), in Jacobs, vol.1, p.110]

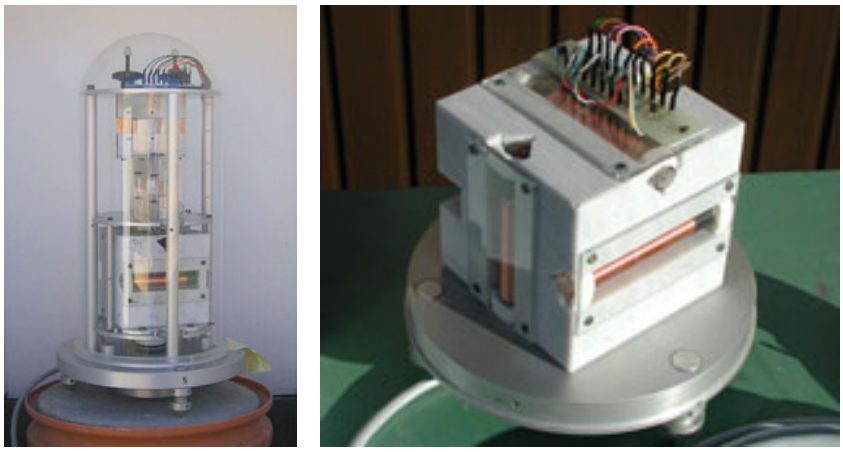

Figure 3.1.5. DMI/DTU Fluxgate magnetometer. Left: in enclosure with cardanic susplension. Right: marble block with 3 orthogonal fluxgate sensors.

Figures 3.1.5a and 3.1.5b illustrates a modern version of the classical fluxgate magnetometer developed at the Danish Meteorological Institute and sold to around 200 observatories all over the world. The instrument has three orthogonal fluxgate sensors mounted in a marble block. It is now produced at the Danish Space Research Institute for sale. (contact Lars W. Pedersen at DTU, lawp@space.dtu.dk).

The group of nuclear resonance magnetometers comprises several different types, among other, the Proton Precession Magnetometer (PPM) and the Rubidium Vapour Magnetometer (RVM). The proton magnetometer principles are illustrated in Fig. 3.1.6. It utilizes the precession frequency of protons, which depends on the strength of the magnetic field. Protons have a magnetic moment that causes them to align their magnetic axes either parallel or anti-parallel to the ambient magnetic field. Typically, the proton magnetometer comprises a bottle with proton-rich fluid such as water or benzene mounted inside a coil. A current impulse through the coil creates an additional magnetic field which causes the proton spin axes to turn into alignment with the new direction of the combined field. When the current is turned off, then the proton spin axes will not immediately return to their original direction but will be precessing for a while. The coil may now pick the (weak) precession signal for

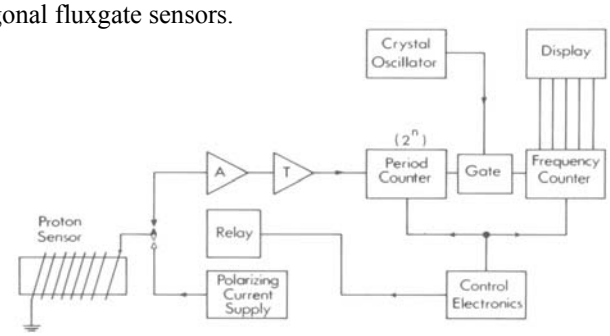

Figure 3.1.6. Proton magnetometer principle. [Forbes (1987), in Jacobs, vol.1, p.87]

analysis of its frequency, fp = $(\gamma_p/2\pi)\cdot B_0$, where $\gamma_p = (q/2mc)$ is the proton gyromagnetic ratio (magnetic moment/angular moment). Thus, the field magnitude is defined solely through atomic constants and the measured frequency through: $B_0 = 23.4874 \cdot f_p$ [nT]

A variant of the simple proton magnetometer is the Overhauser Magnetometer (OHM). Instead of using a pulsating current, the OHM generates the proton precession through resonance excitation of the electron spin at a frequency much higher than the proton precession frequency. The excitation signal can be applied all the time to provide a continuous precession signal that can be filtered to remove the excitation signal.

A different class of nuclear resonance magnetometer is the rubidium magnetometer that uses the Zeemann splitting of atomic energy levels into sublevels where the separation is proportional to the ambient magnetic field strength. The magnetic field-dependent splitting of energy levels is illustrated in Fig. 3.1.7. F and m_F represents the total angular momentum and the resolved magnetic moment. Initially, the ^{85}Rb atoms in a vapour cell are distributed within the $^2S_{1/2}$ ground-state energy levels. If light of wavelength 7946.7Å corresponding to the level shift D_1 is transmitted through the cell, then the photons are absorbed and the atoms are brought to the $^2P_{1/2}$ excited state.

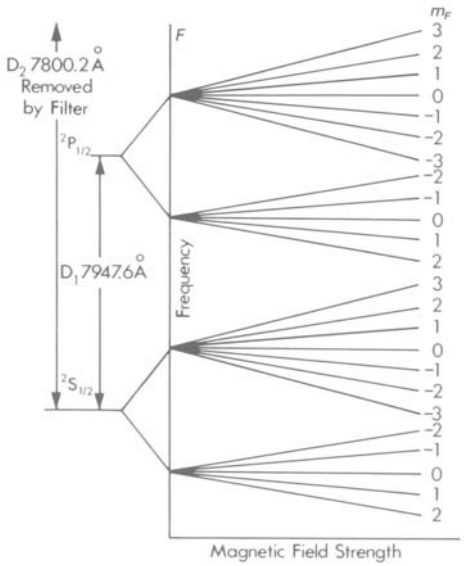

Figure 3.1.7. Zeemann splitting of energy levels. [Forbes (1989), in Jacobs1, p.91]

If the light is right-circularly polarized, then the +1 spin quantum of the photons is transferred to the atom, which experiences a change in m_F of +1 in addition to the D_1 shift. Thus the ground state atoms in the m=+3 sublevel cannot absorb the photon since there is no m=+4 excited level. Similarly, atoms on the m=-3 sublevel cannot absorb a left-circularly photon with -1 spin quantum. When the excited atoms return to the ground state by emitting a photon, the associated transition is 0 or ±1 with equal probability. Hence, an overrepresentation of atoms in ground state sublevel m=±3 results. The gas in the cell is now optically "pumped" and further photons are transmitted with less absorption.

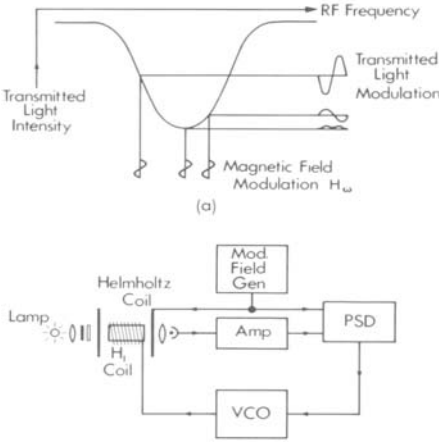

Figure 3.1.8. Locked-oscillator Rubidium magnetometer. [Forbes (1987), in Jacobs, vol.1, p93]

However, the photon absorption rate may be enhanced if a radiofrequency (RF) magnetic field with a frequency corresponding to the energy difference between a pair of sublevels is applied. Then resonantly excited transitions moderate the level splitting such that the enhanced number of atoms "trapped" at sublevels ±3 is brought down.

Fig. 3.1.8. illustrates a "locked oscillator" Rubidium magnetometer. The upper part illustrates the effects of the RF magnetic field, H_1, applied through a coil wound around the Rubidium vapour cell. The amplitude of the transmitted light is modulated by applying a perturbing field, H_ω, perpendicular to the axial field, through the Helmholtz Coil (its cross-section is shown). The phase of the modulation in the transmitted signal shifts by 180° across the resonance. At resonance the modulation signal is double-peaked.

The lower diagram sketches the system. The RF signal is generated by the voltage-controlled oscillator (VCO). The transmitted light signal is detected by a photocell, amplified and fed to a Phase-Sensitive Detector (PSD) along with the modulation signal from the Modulation Field Generator. The DC-output from the PSD unit controls the VCO frequency applied to obtain balance at the level-splitted resonance frequency from which the magnetic field strength can be derived.

3.2. Current systems in the Earth's ionosphere and magnetosphere.

As noted above, the Earths magnetic field measured at the surface holds contributions from external current systems and their induced counterpart in the ground, which amounts from one to a few percents. The strengths and dynamics of the current systems are strongly variable depending, among other, on the region considered. Fig. 3.2.1 illustrates the locations of the magnetically different regions of the Earth.

The map is drawn in geographic coordinates. The equatorial zone (hatched) follows the magnetic equator and has a width of around 10°. Its deviations from geographical equator amount up to + and - 11.2° (dipole tilt).
The northern and southern mid-latitude regions extend up to around 55° geomagnetic latitude where the northern and southern auroral zones (dotted) start. Beyond the auroral zones, the northern and southern polar cap regions extend from around 80° to the geomagnetic poles.

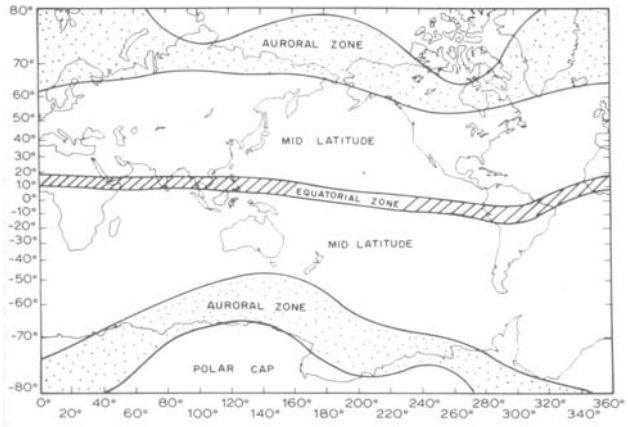

Figure 3.2.1. Earth's magnetic regions. [Rangajaran (1989), p.325]

Solar Quiet Currents. In the absence of disturbances the magnetic field has a fairly regular daily variation linked to the so-called Solar Quiet (Sq) currents generated by the global thermospheric wind system. The upper atmosphere is heated most where the Sun is directly overhead and therefore the air expands to produce motion of the air masses away from the subsolar region. The thermospheric neutral wind system is illustrated in Fig. 3.2.2.

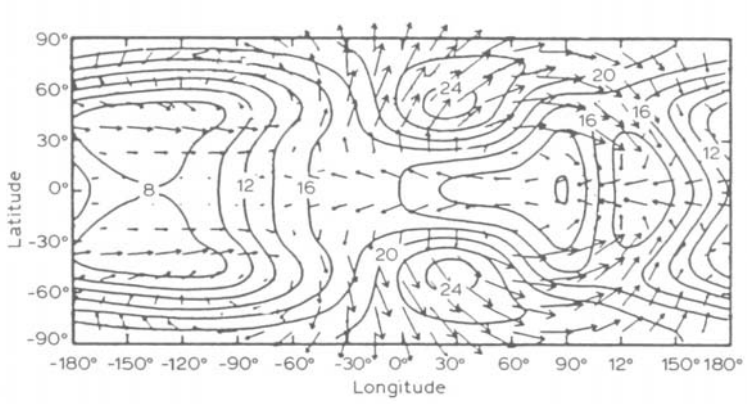

Figure 3.2.2. Thermospheric neutral wind system at 12 GMT. From Fesen et al. (1986). In: Jacobs, vol.3, p.399)

The motion of the air across the Earth's magnetic field induces a **V**x**B** electric field. The thermosphere is partly ionized forming the ionospheric D, E, and F layers. Thus the **V**x**B** field generates electric currents. Close to equator the magnetic field is horizontal. Hence the induced electric field is vertical. Away from equator the magnetic field has an increasing vertical component, downward in the northern hemisphere and upward in the southern and the induced electric field now has a horizontal component.

Around noon and well away from equator in both hemispheres, the regular thermospheric neutral wind system displayed in Fig. 3.2.2 induces westward electric fields that drive horizontal ionospheric currents mainly in the east-to-west direction. In the forenoon sector the fields and currents rotate toward equator while in the afternoon sector they rotate away from equator. The closing return currents flow near equator where they may contribute to form the Equatorial Electro Jet (EEJ) system as the integrated ionospheric conductivity due to the Cowling effect is particularly large where the magnetic field is strictly horizontal. At dip-equator the induced **V**x**B** fields are vertical, but the limited extent of the conducting region inhibits the vertical currents and enhances the horizontal transverse currents. The effective Cowling conductivity, which applies to east-west horizontal electric fields and currents close to magnetic equator, is:

$$\sigma_C = \sigma_1 + \sigma_2^2/\sigma_1 \qquad (3.1.1)$$

Close to dip-equator the integrated Cowling conductivities are much larger than usual mid-latitude conductivities and thus assist to enhance the equatorial electrojet currents.

At night the conductivities are generally much lower due to the strongly reduced electron densities in the E-region, and the resulting ionospheric currents are much weaker than their day-time counterpart. The combined result is the formation of vortex-like Sq horizontal current structures in both the northern and southern hemisphere. The northern and southern Sq current systems are coupled through field-aligned currents from one hemisphere to the other. A simplified sketch of these currents is shown in Fig.3.2.3 (Rangajaran, 1998).

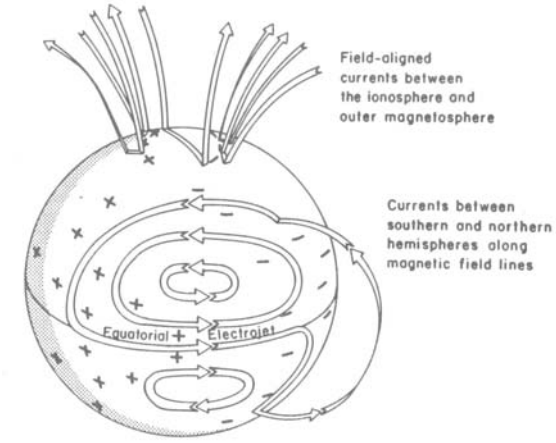

Figure 3.2.3. Simplified sketch of Sq currents. [Rangajaran (1998), p. 264.]

The global system of Sq currents depends on the interaction between thermospheric winds related to the heating of the subsolar atmosphere, the ionisation produced mainly by the solar UV and X-ray radiation, and the geomagnetic field. The global currents have daily variations due to the wobbling of the dipole-like geomagnetic field with respect to the Earth's rotation axis and seasonal variations due to the varying tilt of the axis with respect to the solar ecliptic plane. Furthermore, they depend on the level of ionising solar UV and X-ray radiation and, therefore, they vary with the activity in the 11-year solar cycle. For a geomagnetic observatory the magnetic variations induced by the local Sq currents are reflected in the varying Quiet Level (QL). During a day the variations are sinusoidal-like with respect to local time and constitute the so-called Quiet Day Curve (QDC). The amplitudes in the positive and negative excursions are largest in the summer season and maximises during sunspot maximum in the solar cycle.

SID disturbance currents. The Sq system is activated during solar flare eruptions where the Sun emits enhanced UV and X-ray radiation during a brief interval lasting a few or a few tens of minutes. Usually the strong flares produce hook-like "crochet" signatures with typical amplitudes of 10-100 nT in the magnetic recordings. Such crochets (Solar Flare Event, SFE) are important warning of major solar flares in progress.

Polar and Auroral current systems. The polar and auroral regions are coupled to the outer magnetosphere and to the solar wind. Due to the high conductivity, σ_0 , along the magnetic field in the upper ionosphere and the magnetosphere where the collision frequencies are very low, the field lines could in most cases be considered equipotential structures along which currents may easily flow. An overall view of magnetospheric current systems is provided in the sketch in Fig. 3.2.4. The currents are related to the interaction between the solar wind and the magnetosphere and are mutually coupled.

Fig. 3.2.4 displays (in red) the existence of field-aligned currents, FAC, flowing between the outer magnetosphere and the polar ionosphere. The outermost FAC that connect between the magnetospheric boundary regions and the border of the polar cap are termed "Region 1" currents. Usually, they are downward to the ionosphere in the morning sector and upward from the ionosphere in the evening sector. The inner system of FAC is termed "Region 2" currents. They connect between the ring current magnetospheric region at 4-6 R_E and the low-latitude border of the auroral oval. The directions of the R2 currents are usually upward in the morning sector and downward in the evening sector. The equatorial transverse current connecting between the

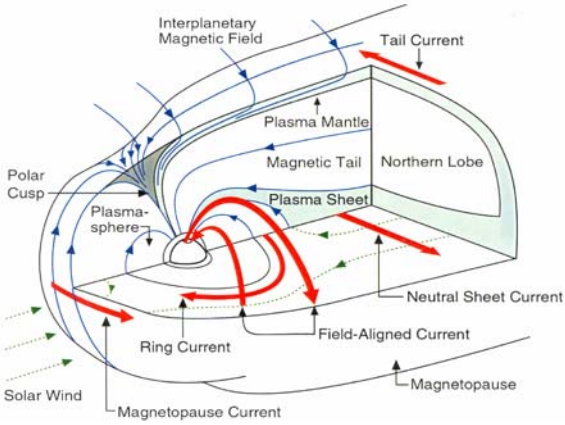

Figure 3.2.4. Sketch of magnetospheric current systems. [after Potemra, 1983, 1984]

morning and evening R2 FAC constitute a partial ring current, which adds to the ring current at the nightside of the magnetosphere. The symmetric ring current is generated by the opposite azimuthal drifts of protons and electrons gyrating in the Earth's magnetic field.

These magnetospheric currents relate closely to the conditions in the solar wind. They are stronger for southward orientation of the interplanetary magnetic field, IMF (negative IMF B_Z) in combination with high solar wind velocities, V_{SW}. The combination could be expressed in terms of a dawn-dusk directed electric field, $E=V_{SW} B_Z$ generated by the relative motion of the Earth with respect to the solar wind.

In addition, currents are flowing in the cusp region between the magnetopause and the ionospheric cusp region located at the dayside at around 75° magnetic latitude in both hemispheres. These currents are termed "Region 0" FAC. They relate specifically to the Y-component of the interplanetary magnetic field, IMF B_Y. Their direction is upward in the northern hemisphere and downward in the southern for positive values of IMF B_Y and opposite for negative IMF B_Y cases. The R0 currents are enhanced at high values of the combination of the IMF B_Y component and the solar wind velocity, V_{SW}. The combination could be expressed in terms of a north-south oriented electric field, $E=V_{SW} B_Y$.

At the morning side in the ionosphere, the downward R1 FAC connect to the upward R2 FAC via horizontal Pedersen currents across the auroral region. Similarly, at the evening side, the upward R1 currents are connected to the downward R2 currents across the evening auroral region. In addition, the downward currents at the morning side are connected to the upward R1 currents at the evening side by currents flowing across the northern and southern polar caps. Depending on their polarity, the R0 currents connect either to the morning or the evening R1 FAC by horizontal Pedersen and Hall currents across the ionospheric cusp region, the so-called "DPY" currents (Disturbance Polar currents related to the Y-component of the IMF).

The ionospheric electric field across the polar cap, which drives the Pedersen horizontal currents, generates convective motion in the upper part of the ionosphere where the collisions are rare. In the almost vertical geomagnetic field, **B**, the ions and electrons have a common **E** x **B** drift velocity. The convection is impeded in the lower ionosphere by frequent collisions between the charged particles and the neutral atmosphere. The ions are first stopped while the electrons may continue their drift motion to lower altitudes. This difference is equivalent to the generation of an electric Hall current opposite of the convection direction. In most cases the convection across the polar cap is antisunward. Hence the polar cap Hall currents are sunward. During cases of strong and northward IMF, the convection and Hall current directions in the central polar cap could be reversed.
Similarly, the horizontal electric fields, which drive the Pedersen currents across the auroral oval between the R1 and R2 FAC systems, generate convection in the auroral ionosphere. The convection is most often sunward and thus the Hall currents are generally antisunward. At the afternoon the Hall currents in the relatively narrow auroral region constitute the eastward auroral electrojet while at the morning side they produce the westward auroral electrojet.

The combination of R1, R2 and R0 field-aligned currents and horizontal polar and ionospheric currents is illustrated in Fig. 3.2.5.

When the possible effects on groundbased magnetic observations are being evaluated, then the Fukushima theorem is very useful. The theorem states that with a horizontally stratified, homogeneous ionosphere, with a system of parallel, infinitely extended, uniform sheets of upward and downward FAC connected by horizontal Pedersen currents, and with induced Hall currents flowing in-between, then the magnetic effects below (outside) the current system will be controlled

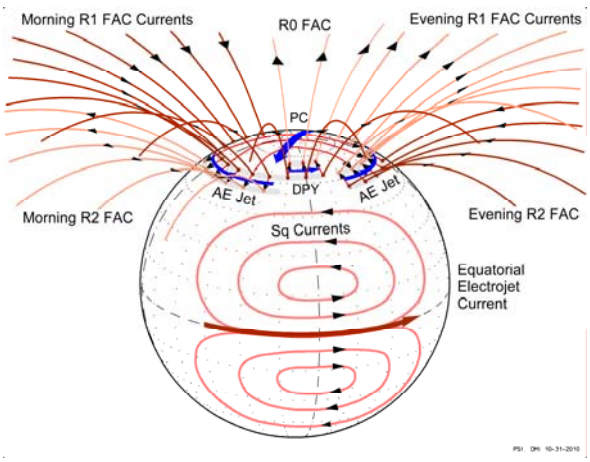

Figure 3.2.5. Field-aligned and ionospheric currents.

by the Hall currents only, since the magnetic effects of the FAC and Pedersen currents cancel each other. The theorem is a fair (not perfect) approximation in most real cases. Thus, the ground magnetic effects in the polar and auroral regions are mainly related to the transpolar and auroral electrojet convection-related Hall currents, respectively.

3.3. Geomagnetic indices.

Some of the accepted geomagnetic indices are directly related to the individual main current systems outlined above. This is the case for the Polar Cap (PCN, PCS), the Auroral Electrojet (AE, AU, AL) indices, the Ring Current (Dst, SYM, ASYM), and the Equatorial Electrojet (EEJ) indices. Another important index type, the K and Kp indices, is more or less related to the combined effects of all disturbance current systems. These indices shall be described briefly in the following.

K and Kp indices. The 3-hourly so-called "K" index was introduced by J. Bartels in 1939 in order to describe the degree of magnetic disturbance (above the regular daily variation) observed in magnetometer recordings. The name (K) was derived from the German word "Kennziffer". The index value is derived from the amplitude range beyond the regular daily variation of the most disturbed of all three magnetic elements (H, D, Z) in a three-hourly interval (00-03, 03-06…UT). The amplitude range can be derived as the distance between the smooth curves of shape equal to the quiet daily curve (QDC) just touching the recorded trace from above and from below. An example is shown in Fig. 3.3.1 (from Rangajaran, 1989).

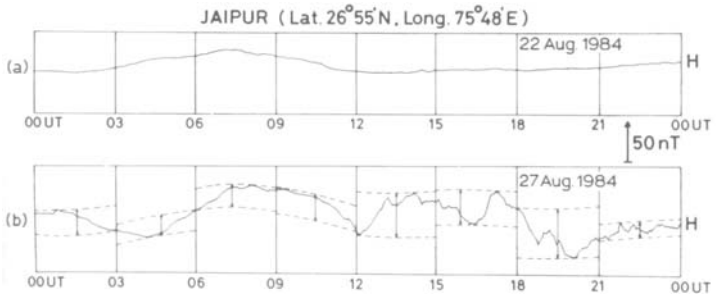

Figure 3.3.1. K-index derivation. [Rangajaran (1989), p.329]

After scaling, the 3-hourly range measured in nT is converted to a single number between 0 and 9 using a scale with logarithmically spaced steps for the amplitude range. The scale is made to depend on the location of the magnetic observatory such that the various grades of activity would give about the same index number irrespective of location. Thus, the K-index value 9 corresponds to ranges above 300 nT for a mid-latitude station (very strong storm) while an for auroral zone station a K-index value 9 corresponds to ranges above 1500 nT (also very strong storm). At that location a range of 300 nT would correspond to a mild magnetic storm. Over time the distribution of K-index values should be the same for all observatories independent of their location.

Based on the average of local K-indices from a selected group of mid-latitude, high-quality magnetic observatories a planetary K-index, Kp is constructed. The Kp index has a good longitudinal coverage and is thus sensitive to global magnetic disturbances regardless of the time of day. The Kp index may indicate disturbances originating both in Sq-type of magnetic variations (e.g., Solar Flare-related crochets), auroral electrojet variations (e.g., substorms), and ring current variations (magnetic storms).

The Kp index is often used in data analyses to indicate the general level of global magnetic disturbances, for instance, in the definition of undisturbed intervals for selection of data for construction of the quiet day variation (QDC) for magnetic recordings. It should be noted, however, that the Kp index is valid only to define mid-latitude disturbances. In the central polar cap, the disturbance level could be high during cases of northward IMF even at times with low Kp values.
The final Kp index values are calculated at GeoForschungs-Zentrum (GFZ) in Potsdam (http://www-app3.gfz-potsdam.de/kp_index/index.html) .

Kp=9	G5
Kp-index	NOAA Space Weather Scale Geomagnetic Storm Level
Kp=5	G1
Kp=6	G2
Kp=7	G3
Kp=8	G4

On-line real-time preliminary Kp values are issued by NOAA Space Weather Prediction Center (http://www.swpc.noaa.gov/rt_plots/kp_3d.html) on basis of data from a limited selection of observatories in the North American sector. The preliminary Kp index values are used to specify the severity, G0 – G5 of possible geomagnetic storm conditions according to the table.

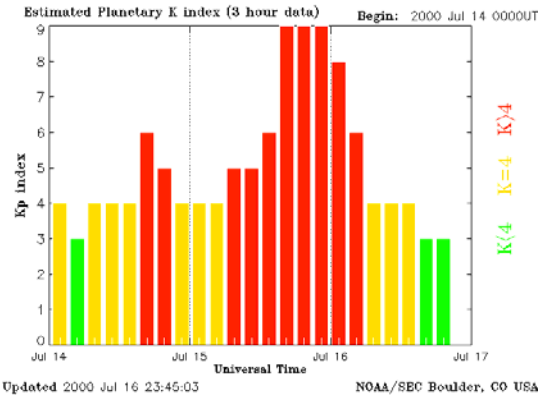

Figure 3.3.2. Real-time Kp index values during the Bastille storm event starting 14 July 2000. NOAA SEC web site: http://www.swpc.noaa.gov/rt_plots/kp_3d.html

From that source, an example of the NOAA real-time preliminary Kp index series for a large storm is shown in Fig. 3.3.2. The diagram presents Kp index values for a 3-days interval. The latest values are automatically inserted as they become available. The example event ("Bastille event") started with an X-ray flare of class X (very large) at 10 UT on 14 July, 2000, and it was accompanied by a very intense radiation of high-energy solar protons.

The 3-hour Kp "sample" duration could be too long for use of the Kp index in real-time Space Weather Forecast services. A more direct access to the raw magnetometer data might be preferable for such purposes.

Auroral Electrojet Indices, AU, AL, AE, AO. The auroral electrojet indices were developed by Davis and Sugiura (1966) to characterize the strength of the eastward and westward electrojet currents. In the northern hemisphere, the eastward electrojet current in afternoon sector of the auroral oval would produce enhancements (i.e., positive variations) of the northward magnetic component in that region. Correspondingly, the westward electrojet current in the morning sector would produce reductions (i.e., negative variations) of the local northward magnetic component. The index is based on measurements of the horizontal magnetic component from a range of observatories located in the auroral zone and well distributed in longitude.

The AU and AL index values are defined as the amplitudes in nT of the upper and lower envelope, respectively, of the ensemble of magnetic recordings corrected for the regular daily variation (QDC). Thus the AU values are mostly defined from observations in the afternoon sector of the auroral oval while the AL values are defined from the magnetic data from the morning sector of the oval. The AE values are defined as the difference, AE = AU – AL, while the AO index values are defined as the average, AO = 0.5 (AU + AL). Initially, the index values were calculated as 2.5 min samples. Now, they are also provided at 1-min resolution. Presently, the basic net of stations comprises 12 observatories.

The auroral electrojet indices are calculated by the World Data Center (WDC-C2) in Kyoto, Japan (http://wdc.kugi.kyoto-u.ac.jp/aedir/index.html). Real-time index values are provided on-line from the Kyoto data center in numerical or graphical form on basis of raw data from the available observatories.

A recent example of actual on-line real-time AU, AL, AE, and AO index data is displayed in Fig. 3.3.3. from the web site: http://wdc.kugi.kyoto-u.ac.jp/aedir/index.html .

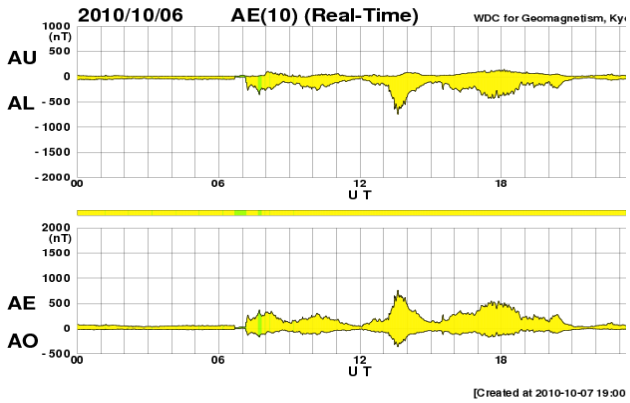

Figure 3.3.3. Real-time AE values based on 10 stations. From Kyoto WDCC2 web site.

In the ESA SWENET project, GIFINT at http://gifint.ifsi.rm.cnr.it/, a neural network algoritm is used for 1-hr forecast of the AE index based on ACE satellite data (http://www.srl.caltech.edu/ACE/). For such real-time forecasts based on ACE satellite data it is important to take into account that the satellite or its instruments (e.g., the solar wind detectors) could be disabled by the high-energy radiation that often accompanies solar flares and coronal outbursts (CMEs).

Dst index. The Dst (Disturbance Storm Time) is a geomagnetic index, which monitors the world wide magnetic storm level. The index represents the axially symmetric disturbance magnetic field at the dipole equator on the Earth's surface. Major disturbances in Dst are negative, namely decreases in the geomagnetic field. These field decreases are produced mainly by the equatorial current system in the magnetosphere, usually referred to as the ring current, which flows clockwise around the Earth in the equatorial plane. The ring current results from the differential gradient and curvature drifts of electrons and protons in the near Earth region and its strength is coupled to the solar wind conditions. The neutral sheet current flowing across the magnetospheric tail makes a small contribution to field decreases near the Earth. Positive variations in Dst are mostly caused by the compression of the magnetosphere from solar wind pressure increases (e.g., at SSC at the arrival of the front of a CME). Negative Dst values indicate a magnetic storm is in progress (e.g., the main phase during CME events), the more negative Dst is the more intense the magnetic storm.

A starting point for the studies concerning Dst derivation came at the end of the forties, when J. Bartels, chairman of the Committee on Characterization of Magnetic Disturbances of IATME and IAGA, stimulated studies for deriving an index to monitor the equatorial ring current variations. Preliminary attempts for defining such an index were made at the end of the fifties and the beginning of the sixties (e.g., Sugiura, 1964). A derivation scheme developed by Sugiura and co-workers was adopted by IAGA (Resolution 2, p. 123, in IAGA Bulletin 27, Madrid, 1969).

In principle, the Dst index is constructed by averaging the horizontal component of the geomagnetic field from low-latitude magnetograms from all over the world. Presently, the Dst index is derived from five magnetic observatories, Hermanus, Kakioka, Honolulu, San Juan, and Alibag. These observatories were chosen on the basis of the quality of observations and for the reason that their locations are sufficiently distant from both the auroral and equatorial electrojets and that they are distributed in longitude as evenly as possible. The baseline for H is defined for each observatory in a manner that takes into account the secular variation. For each observatory, the annual mean values of H, calculated from the "five quietest day" for each month, form the database for the baseline. It should be remembered that the final Dst values are determined after each calendar year and that therefore in this determination, the annual mean values are available only up to and including the year (referred to as the “current” year) for which the final Dst is to be deduced.

The Dst values are calculated by the WDC-C2 in Kyoto and made available at their web site (http://wdc.kugi.kyoto-u.ac.jp/dstdir/index.html). Real-time preliminary Dst values are available on-line at the link: http://wdc.kugi.kyoto-u.ac.jp/dst_realtime/presentmonth/index.html . An example of recent Dst values are given in the plot for October, 2010, in Fig. 3.3.4.

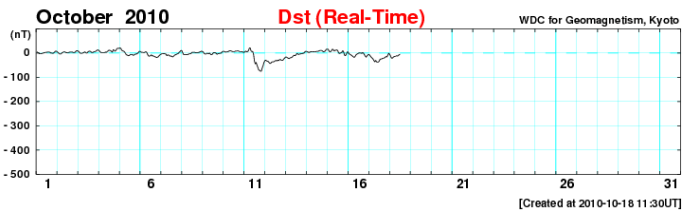

Figure 3.3.4. Real-time Dst index for October 2010. Note the minor storm on 11-12 October. From Kyoto WDC-C2 web site.

Various attempts have been made to forecast Dst index values from measurements of solar wind parameters. Burton et al. (1975) found that the Dst index could be predicted quite successfully using the following formula.

$$d(Dst^*)/dt = F(E) - a\,Dst^* \qquad (3.3.1)$$

where

Dst* = Dst - b sqrt(Pdyn) + c,
F(E)= d (Ey-0.5) for Ey>0.5 mV/m or else F(E)=0.
a = 3.6×10^{-5} /s
b = .20 nT/$\sqrt{(eV/cm^3)}$
c = 20 nT
d = -1.5×10^{-3} nT/(s mV/m)

In this equation Dst* is the amount of Dst from the injected ring current only. The constant b is a measure of the Dst response to solar wind dynamic pressure ($Pdyn=m_{SW}N_{SW}V_{SW}^2$) while c is a measure of the quiet time ring current. F(E) is the ring current injection rate and depends only upon the dawn to dusk solar wind electric field, Ey, which is just the negative product of the solar wind speed, V_{SW}, and the southward component, Bz, of the interplanetary magnetic field. The constant d is a measure of the response of the injection rate to Ey, which is assumed to be linear, and the parameter a is a measure of ring current decay, the value of which corresponds to an e folding time of 7.7 hours. Updated calculations of the predicted Dst index using ACE satellite data (http://www.srl.caltech.edu/ACE/) and a slightly improved formula are available at: http://sprg.ssl.berkeley.edu/dst_index/images/cumulative.gif .

A neural network algoritm is used for 1-hr forecasts of Dst based also on ACE satellite data in the ESA SWENET project, GIFINT. The results are available at http://gifint.ifsi.rm.cnr.it/. As noted above, it is important to take into account that the satellite or its instruments (e.g., the solar wind detectors) could be disabled by the high-energy radiation that often accompanies solar flares and CME outbursts. An example of real-time data from ACE from 15 July 2000 is shown in Fig. 3.3.5. Note the depression of VSW up to 16 UT on 15 July 2000. The depression was caused by the radiation of high-energy solar protons emitted from the active flare region starting at 10 UT on 14 July 2000 (the "Bastille Event").

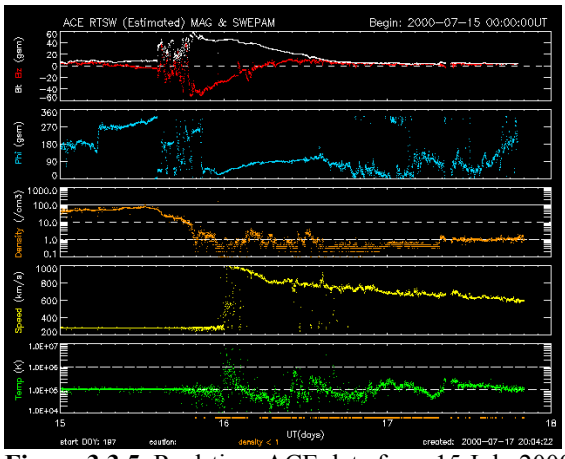

Figure 3.3.5. Real-time ACE data from 15 July 2000. Note the radiation-related depression of V_{SW} up to 16 UT. From ACE web site.

A feature of importance both for scientific analyses and for the use of the Dst index in Space Weather forecast project is the 1-hour "sample" time for index values. At WDC-C2 the magnetic data received from the stations are now in 1-min Intermagnet digital format. Hence the Dst index could, in principle, be derived in 1-min resolution. The magnetic data from the Dst observatories and a few additional mid-latitude observatories are processed to derive 1-min values of the symmetrical and the asymmetrical variations in H and D. The 1-min samples of the symmetrical part of the H- or D-components are termed SYM ("symmetrical") values since they, like the Dst index, represent the symmetrical part of the ring current disturbances. The SYM-H value is close to being a Dst index in 1-min resolution. The ring current (RC) and the associated magnetic variations also have an asymmetrical part attributed mainly to the partial ring current (PRC) and neutral sheet tail current (TC). The ASYM asymmetrical H- or D-component values are derived from the 1st order harmonic expansion terms. Final values of the SYM and ASYM data are available from the WDC-C2 ftp-server. Real-time values are not yet available. However, they could be derived with fair accuracy either from solar wind data (e.g., ACE satellite) or from polar cap index values.

Polar Cap Indices, PCN and PCS. The polar cap indices, PCN for the northern polar cap and PCS for the southern, are mainly determined by the intensity of the antisunward transpolar convection-related Hall current system with minor contributions from the auroral electrojet currents. Presently they are derived from

the magnetic recordings made at Thule (PCN) and Vostok (PCS) following a scheme originally devised by Troshichev et al. (1988). The basis for the index is the assumption that the transpolar convection and hence the Hall currents are mainly driven by the so-called "geo-effective" (or "merging") solar wind electric field (Kan and Lee, 1979):

$$E_m = V_{SW} B_T \sin^2(\theta/2). \qquad (3.3.2)$$

This parameter is a combination of the solar wind velocity, V_{SW}, and the transverse component, B_T, ($B_T = (B_Y^2+B_Z^2)^{1/2}$) of the interplanetary magnetic field (IMF) and includes a strong dependence on the field direction represented by the polar angle θ of the transverse component with respect to the Z-axis in a Geocentric Solar Magnetospheric (GSM) coordinate system (i.e., $\tan(\theta)=|B_Y|/B_Z$, $0 \le \theta \le \pi$). An example of polar cap electric potential, convection and magnetic disturbance patterns are provided in Fig. 3.3.6 (after Friis-Christensen et al., 1985). The arrow indicates the direction of the magnetic variation, **ΔF** .

At ground level the uniform transpolar currents generate horizontal magnetic variations, **ΔF,** that are perpendicular to the current direction. In order to enhance the relations to the solar wind geo-effective electric field and suppress other contributions, then the magnetic disturbance vectors are projected to a so-called "optimum direction" derived by searching optimum (statistical) correlation between the scalar value, ΔF_{PROJ} , of the projected vector and E_m . From (statistical) regression analysis the best linear fit between ΔF_{PROJ} (in nT) and E_m (in mV/m) is determined:

$$\Delta F_{PROJ} \sim S \cdot E_m + \Delta F_I \qquad (3.3.3)$$

where S is the "slope" and ΔF_I the "intercept". Now, this equation is inverted to provide an estimate of the parameter, PC, that result from using actual values of the projected magnetic variations:

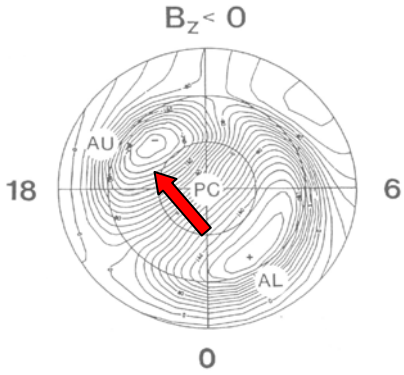

Figure 3.3.6. Polar Cap potential and convection contours during Bz < 0. From Friis-Christensen et al., 1985

$$PC = (\Delta F_{PROJ} - \Delta F_I)/S \quad (\sim E_m \text{ [in mV/m]}) \qquad (3.3.4)$$

The three parameters, optimum angle, slope and intercept, are determined over a span of years and are, for instance, provided in tables of hourly values for each hour of the day and each month of the year from which values for any given day and time of day could be derived by interpolation. In the original concept the magnetic variations were counted from the base-line set by the "internal" field components. In a recent scheme (Troshichev et al., 2006), the magnetic variations are now counted from the quiet level (the QDC).

The PC indices are usually provided in 1-min resolution. They are not (yet) adopted as official IAGA indices, the approval is pending. PCN index values (1975-2009) are available on request from the Danish Meteorological Institute, DMI, (pst@dmi.dk). Graphical displays of recent PCN values are available at http://wdcc1.dmi.dk/pcnu/pcnu.html. PCS index values (1996-2010) are available from the Arctic and Antarctic Research Institute (AARI) in St. Petersburg, Russia (olegtro@aari.nw.ru). Recent PCS values are displayed on-line at http://www.aari.nw.ru/clgmi/geophys/pc_main.htm . An example is shown in Fig. 3.3.7:

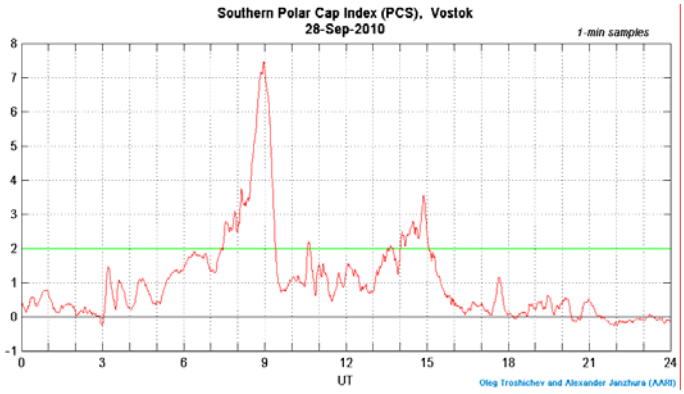

Figure 3.3.7. On-line PCS index at AARI web site

The PC index can be considered a proxy for the geo-effective solar wind electric field, E_m. The E_m parameter is considered the best indicator of the transfer of energy from the solar wind to the Earth's magnetosphere. The energy is used, among other, to sustain ionospheric currents and associated Joule heating via the R1 and R0 FAC, to create the magnetospheric stresses that are released in substorms, and to build the ring current system. These effects can also be derived to a fair approximation by using the polar cap indices, PCN and PCS, rather than the solar wind electric field, Em, in calculations. For the build-up of stresses to be released in substorms the PC index may be used to predict the substorm onset. If the PC index increases from near zero but only has values below 2 then a substorm may arrive with an onset delayed by 10-30 min with respect to the rise in the PC index. If the PC index exceeds 2 then a substorm will follow within 5-10 min. If the PC index takes still larger values then substorm activity will start immediately.

In calculations of the equivalent Dst ring current index using the above Burton et al. (1975) formula, the PC indices may provide as fair an approximation to the real Dst index values as the solar wind E_m. An example is shown in Fig. 3.3.8 for the large October 2003 storm. The Dst index is shown in black line with dots. The solar wind electric field and the derived Dst index in red. The PC index in blue and the derived Dst index in blue line with dots. The strong solar proton radiation disabled the ACE solar wind velocity instrument at an early time in the event. Hence the Em and the equivalent Dst values derived from Em are missing during most of the event. The same adverse conditions apply to forecast calculations of the auroral electrojet indices.

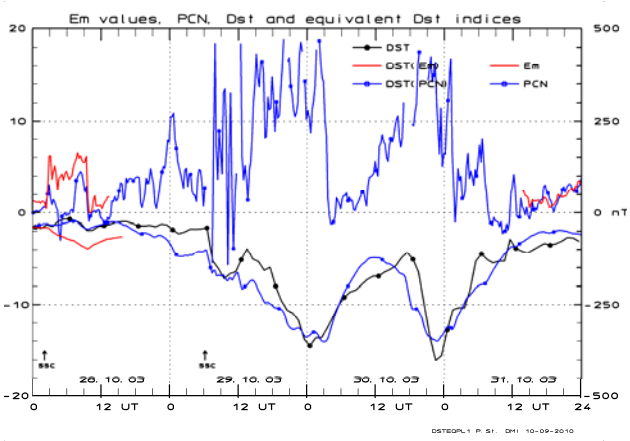

Figure 3.3.8. Em, PCN, Dst and equivalent Dst during storm. (Stauning, 2008)

For the really strong solar events (like the Carrington or Bastille events), the solar wind speed may rise to around 2000 km/s during the initial phase of the event. With this speed the coronal ejecta may reach from the ACE satellite to the Earth in less than 15 min. Thus, the time difference between ACE-based and PC-based forecasts of possible effects (e.g., warning of GICs) is quite small. Bearing in mind the possibility that the satellite or its instruments could be impaired by the accompanying solar high-energy proton radiation, makes a real-time on-line PC index attractive to provide an alternative source for warnings or verifications of adverse Space Weather conditions.

Space Weather problems related to magnetic variations. The two most serious problems related to geomagnetic variations are power grid disturbances and pipeline corrosion. Both are related to the Geomagnetically Induced Currents (GIC) that flow in all conducting structures at variations in the ambient magnetic field. For such currents to pose a threat to technical systems the magnetic variations need to be large and fast to produce strong flux variations, and the conducting structures need to have a substantial extension to form induction loops of considerable size. The first condition is met in and equatorward of the auroral regions since only auroral electrojet-types of currents have the strength and variability needed to produce significant GIC effects. The second condition is met by extended high-voltage lines in power grid systems and by long pipelines for oil and gas. Earlier, DC-coupled systems like telegraph lines and railroad signal lines were also vulnerable (e.g., during the Carrington storm) but modern techniques (e.g., AC-coupling, fibre-optical cables) have solved such problems.

The eastward and westward auroral electrojet currents are sustained by R1 and R2 field-aligned currents usually originating in the magnetospheric boundary regions. However, during magnetospheric substorms strongly enhanced field-aligned currents may emerge from the unstable and dynamic regions in the magnetospheric tail to produce localized and very intense electrojet currents in the ionosphere at the

nightside of the auroral zone. The substorms are particularly intense during events of high-speed solar wind flow and strong southward IMF, which may occur when the Earth is targeted by solar coronal mass ejection (CME) events. During the stronger events, the auroral substorm activity expands equatorward. Hence, the regions particularly exposed to strong and sudden magnetic variations are not the usual auroral zone location but the regions extending a few (~5-10) degrees equatorward.

Illustrative examples of GIC problems in power grids are provided by the events of disturbances in the high-voltage (HV) power lines connecting the hydro-electric power plants located in Northern Sweden at the equatorward edge of the normal auroral zone to the consumers in the southern part of Sweden. Fig. 3.3.9 sketches the principal features .

An induction loop is formed between the wires of the HV line terminated through transformers in both ends and effective ground at some depth. In the ionosphere at around 100 km altitude a variable electrojet current is flowing. The flux variations within the loop induces an emf that may either produce excessive "null-currents" in the transformers if they are grounded or spurious high voltages if they are isolated from ground.

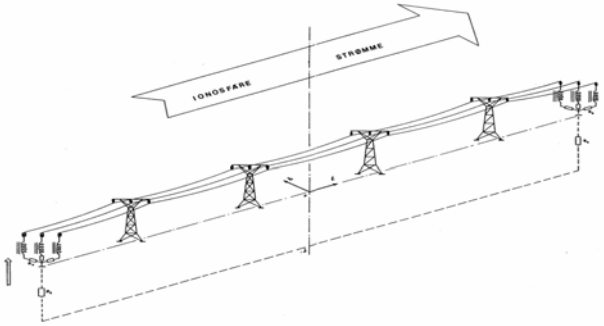

Figure 3.3.9. Sketch of auroral electrojet and HV power line. (From Stauning, 2001. In ESA SP477, pp. 521-524, 2002)

In the first case the transformer core could be saturated such that the usual power line currents now will heat the transformer. In both cases the over-voltage or null-current control systems may trip and cause the unit to be disconnected. Fig 3.3.10 presents examples of power line problems occurring during the great magnetic storms in 1982, and 1989. The PCN index values are displayed in the upper panels. The middle panels display the auroral electrojet indices AU (blue) and AL (red line) while the lower panel shows the horizontal (H) component of the magnetograms from Brorfelde in Denmark. Power line disruptions in Sweden are marked by black triangles.

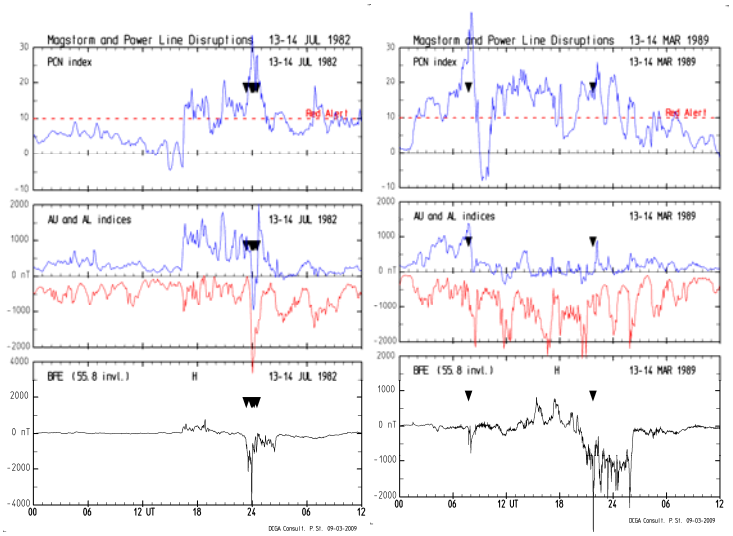

Figure 3.3.10. Examples of PCN, AU, and AL variations, magnetic recordings at Brorfelde and high-voltage power line disruptions marked by triangles in Sweden during large magnetic storms. From Stauning, 2009.

It is evident in Fig. 3.3.10 that the large and sudden magnetic disturbances indicated by the excursions particularly in the AL index occur during enhanced PCN index values above 10 ("red alert"). Not all substorms (indicated by deep excursions in AL) cause large deflections in the magnetograms from Brorfelde located just south of the HV power lines in question. The large and rapid local magnetic disturbances and the related power line disruptions are only seen when the Scandinavian longitude sector happens to be located in the night sector. Otherwise the corresponding disturbances associated with the large AL, AU excursions may hit another longitude sector.

Links and further reading:

Kp from NOAA Space Weather Prediction Center: (http://www.swpc.noaa.gov/rt_plots/kp_3d.html
Kp from GeoForschungs-Zentrum (GFZ), Potsdam (http://www-app3.gfz-potsdam.de/kp_index/index.html)
AE, Dst indices from WDC-C2 in Kyoto: (http://wdc.kugi.kyoto-u.ac.jp/dstdir/index.html).
Real-time Dst values on-line: http://wdc.kugi.kyoto-u.ac.jp/dst_realtime/presentmonth/index.html .
ACE satellite data: http://www.srl.caltech.edu/ACE/
Improved Dst formula: http://sprg.ssl.berkeley.edu/dst_index/images/cumulative.gif .
Recent PCS values: http://www.aari.nw.ru/clgmi/geophys/pc_main.htm
ESA SWENET project, GIFINT: http://gifint.ifsi.rm.cnr.it/.
General Space Weather data: http://www.swpc.noaa.gov/today.html#satenv

Magnetic data links
International Monitor for Auroral Geomagnetic Effects (IMAGE): http://www.ava.fmi.fi/image/data.html
Nordic magnetometer data at Tromsø Geophysical Observatory (TGO): http://geo.phys.uit.no
Realtime data: http://flux.phys.uit.no/geomag.html, http://flux.phys.uit.no/stackplot/
Russian magnetometer data: http://www.aari.nw.ru/clgmi/geophys/pc_main.htm
210˚ Magnetic Meridian real-time data: http://magdas.serc.kyushu-u.ac.jp/qdata/index.php
Geophysical Institute Magnetometer Array (GIMA): http://magnet.asf.alaska.edu
Magnetometer Array for Cusp and Cleft Studies (MACCS), Realtime dataplots:
http://space.augsburg.edu/space/MaccsHome.html
Boulder Magnetometer realtime: http://www.swpc.noaa.gov/rt_plots/bou_12h.html
Time History of Events and Macroscale Interactions During Substorms (THEMIS):
http://themis.ssl.berkeley.edu
Canadian Magnetic Observatory System (CANMOS) data: http://gsc.nrcan.gc.ca/geomag/data/index_e.php
Realtime data: http://geomag.nrcan.gc.ca/common_apps/auto_generated_products/stackplot_e.png
SuperMAG: http://supermag.jhuapl.edu/index.html
SuperMAG data base: http://supermag.jhuapl.edu/inventory/index.html

Reference book:
J. A. Jacobs (editor): Geomagnetism. Vol. 1-4. Academic Press Ltd. 1987-1991.

Main field models:
Langel, R. A. (1987), The Main Field, in: Geomagnetism, vol. 1, ed.: J. A. Jacobs, pp.249-512.

Magnetic instruments:
Forbes, A. J. (1987), Generel Instrumentation, In: Geomagnetism, vol. 1, ed. J. A. Jacobs, pp. 52.142.

Indices:
Rangarajan, G. K. (1989), Indices of Geomagnetic Activity, In: Geomagnetism, vol.3, ed.: J. A. Jacobs, pp.323-384.

4. Ionospheric radiowave propagation.

4.1. Ionospheric refractive index. The propagation of electromagnetic waves in the ionospheric regions is controlled by the refractive properties of the ionized medium (plasma). In a simplified version these properties are described by the so-called Appleton-Hartree formulas.

An electromagnetic signal transmitted through a plasma sets the electrons in motion corresponding to the variations in the wave field. The energy thus accumulated in the electron motion is re-radiated to be added to and restore the wave field. Thus, the wave only looses energy if the electrons collide with heavier particles whereby their organized motion is disturbed.

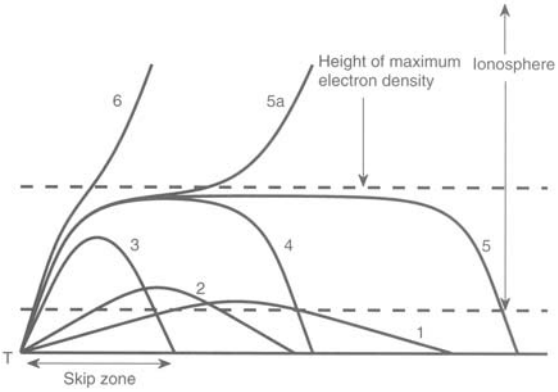

Figure 4.1.1. Refraction of waves in the ionosphere. From K. Davies, 1966. In: Levis et al., 2010, p. 265

A plane, harmonic electromagnetic wave, where the transverse electric and magnetic field components vary as exp(i(ωt-kx)), will create polarization, **P**, in an ionized medium by causing the electrons to move around their equilibrium positions at the wave frequency. The resulting displacement field, **D**, is thus:

$$\mathbf{D} = \varepsilon_0\mathbf{E} + \mathbf{P} = \varepsilon\mathbf{E} \qquad (4.1.1)$$

The phase speed of the wave is:

$$v_{ph} = 1/(\varepsilon\mu_0)^{½} \qquad (4.1.2)$$

and the refractive index is:

$$n^2 = (c/v_{ph})^2 = \varepsilon/\varepsilon_0 = 1 + \mathbf{P}/(\varepsilon_0\mathbf{E}) \qquad (4.1.3)$$

For a medium with free electrons and no external magnetic field, the electron equation of motion in the harmonic wave field takes the form:

$$m_e d^2x/dt^2 = qE - m_e\upsilon dx/dt \quad \rightarrow \quad -m_e\omega^2 x = qE - m_e\upsilon i\omega x \qquad (4.1.4)$$

where x denotes the transverse electron motion, m_e is the electron mass, q is the electron charge and υ its effective collision frequency.

Solving for the polarization, $P=qN_ex$, gives:

$$P = -N_eq^2E/(m_e\omega^2 - m_e\upsilon i\omega) \qquad (4.1.5)$$

Introducing now the plasma frequency $\omega_p^2=N_eq^2/\varepsilon_0m_e$, and the dimensionless quantities $X=\omega_p^2/\omega^2$ and $Z=\upsilon/\omega$ gives for the refractive index:

$$n^2 = (\mu - i\chi)^2 = 1 - X/(1-iZ) \qquad (4.1.6)$$

where the refractive index is now divided in a real part, μ, and an imaginary part, χ. The real part is primarily responsible for the changes in the wave phase and group velocities while the imaginary part is related to the collisional damping of the wave.

The real part of the refractive index has a null when the wave frequency equals the plasma frequency. The phase velocity goes to infinity while the group velocity goes to zero. For a situation where the wave enters a medium with gradually increasing electron density (i.e., increasing plasma frequency) then the signal is reflected at the level where its frequency reaches the local plasma frequency.

Turning now to the real ionosphere with a stationary magnetic field, **B**, then the propagation of electromagnetic (e.g., radio) waves gets much more complicated. Now, the electrons no longer can be assumed to move freely since they are constrained to gyrate in the magnetic field at the gyro frequency $\omega_b=qB/m_e$. Thus the effects on the electron motion from the wave field depend on the direction of wave propagation with respect to the stationary magnetic field and on the wave polarization, for instance, whether the wave field rotates the same way as the electron gyro motion or the opposite way.

Introducing the dimensionless quantities $Y = \omega_b/\omega$, $Y_L = Y\cos\theta$, and $Y_T = Y\sin\theta$, where θ is the angle between the stationary magnetic field and the propagation direction, in the electron equation of motion to solve for the polarisation in the medium then two solutions appear, one for each characteristic wave polarisation. If P1 is the (medium) polarization in the plane extended by the magnetic field and the propagation direction and P2 is the polarization perpendicular to this plane, then the equation for the polarization ratio, R, has two solutions:

$$R=\frac{i}{2\,Y_L}\left\{\frac{Y_T^2}{(1-X-iZ)}\mp\sqrt{\frac{Y_T^4}{(1-X-iZ)^2}+4\,Y_L^2}\right\} \qquad (4.1.7)$$

which, when used in the wave equation to derive the complex refractive index, gives the Appleton-Hartree formula:

$$n^2=1-\frac{X}{1-iZ-\dfrac{Y_T^2}{2(1-X-iZ)}\pm\sqrt{\dfrac{Y_T^4}{4(1-X-iZ)^2}+Y_L^2}} \qquad (4.1.8)$$

If collisions are neglected (Z=0) then the equation for refractive index has a much simpler real form:

$$\mu^2=1-\frac{2X(1-X)}{2(1-X)-Y_T^2\pm\sqrt{Y_T^4+4(1-X)^2Y_L^2}} \qquad (4.1.9)$$

The refractive index has zeros (total reflection) for the following conditions:

With + sign:	X = 1	(ordinary wave: “O”)	(4.1.10)
With – sign:	X = 1-Y	(extraordinary wave: “X”)	
	X = 1+Y	(extraordinary wave: “Z”)	

For signals transmitted into an ionosphere of increasing electron density, the reflection condition (μ=0) is first met at the layer where X=1-Y (“extraordinary” wave). Then the other characteristic wave termed the “ordinary” wave is reflected at X=1 which is the same reflection condition as that found in the case without magnetic field. The reflection condition X=1+Y will apply higher up for still greater electron density, but usually the extraordinary wave is already reflected at a lower height. During turbulent conditions and when the magnetic field is vertical the X=1+Y reflection condition could be met.

The feature that the ionosphere is double refracting implies that an incoming wave field is usually split into two characteristic waves that travel independently through the medium. They may be bended and damped differently and may be reflected at different heights. The distribution of signal power into each of the two

characteristic waves depends on the initial polarization of the wave field. If the initial polarization happens to match one of the two characteristic polarizations then the wave field propagates as a single characteristic wave.

4.2. Absorption. Electromagnetic (radio-) waves passing through an ionized medium are absorbed when the electrons set in motion in the wave field are disturbed by collisions and thus prevented from re-radiating the accumulated wave energy. The absorption may be derived from the general formula for the complex refractive index. Using for the refractive index the simple formula that neglects the magnetic field gives for the complex refractive index:

$$n^2=(\mu-i\chi)^2=1-\frac{X}{1-iZ}=1-\frac{X}{1+Z^2}-\frac{iXZ}{1+Z^2} \qquad (4.2.1.)$$

For a wave travelling in the x_1 direction the wave field is:

$$E=E_0\exp i\left(\omega t-\frac{\omega}{c}nx_1\right) \qquad (4.2.2.)$$

Hence, with a complex refraction index, the field can be written as the product of an infinite plane wave and an exponentially decaying factor:

$$E=E_0\exp\left(-\frac{\omega}{c}\chi x_1\right)\exp i\left(\omega t-\frac{\omega}{c}\mu x_1\right) \qquad (4.2.3.)$$

The decay of amplitude in unit distance is called the absorption coefficient $\kappa = \chi\omega/c$ and is now found by equating the imaginary terms of the above expression for the refractive index and inserting the parameters for X and Z:

$$\kappa=\frac{\omega}{c}\frac{1}{2\mu}\frac{XZ}{1+Z^2}=\frac{e^2}{2\epsilon_0 mc}\frac{1}{\mu}\frac{N\nu}{\omega^2+\nu^2} \qquad (4.2.4.)$$

Usually, the collision frequencies are much smaller than the wave frequencies of interest for transmission services (i.e., $\nu<<\omega$). Hence absorption processes are particularly important either when the collision frequencies, ν, are large even when the electron densities, N, are rather low such that the refractive index, μ, is near unity (non-deviative absorption) or for moderate collision frequencies when the electron densities are large enough to cause the refractive index to approach zero (deviative absorption).

Collision processes are more frequent in the denser atmosphere in the lower part, the D-region, of the ionosphere than higher up. Still lower (below the D-region) the electron number is too small to significantly absorb energy from propagating waves. Hence the non-deviative absorption processes maximizes in the D-region at altitudes of around 60-90 km. The deviative absorption processes are particularly important in the regions where the signals are refracted (or reflected).

During normal (undisturbed) conditions the D-region is weakly ionized by the solar UV- and soft X-ray radiation. The ionization of NO (a minor constituent) by radiation at the Lyman-α (1215Å) line is particularly important. It is seen from the equation for κ that for $\nu<<\omega$, the non-deviative absorption is proportional to the product of the electron density N and the collision frequency and inversely proportional to the square of the wave frequency (i.e., $\kappa = \text{const. } N\,\nu / \omega^2$).

Taking into account the electron velocity distribution gives a more complicated formula for the absorption coefficient, but the general features remain the same. If the magnetic field is included then the expression for the absorption coefficient gets very complicated. However, for many purposes at high frequencies, the absorption coefficient could be derived from the simple expression in a fair approximation by using the modified frequencies $f' = f \pm f_b \cos\theta$ where θ is the angle between the ray direction and the magnetic field.

4.3. Ionospheric scatter processes. Scattering of electromagnetic waves from irregularities in an ionized medium is en extremely important process. For many transmission services scattering processes are the most important environmental problem. Furthermore, scatter processes are the fundamental basis for many important diagnostic techniques for ionospheric investigations, for instance coherent and incoherent scatter radars. There are several types of scattering processes, for instance, scattering from sharp transitions in the refractive index on length scales comparable to the signal wavelength. However, the most important scatter process for many ionospheric radio wave propagation applications is the Bragg scattering. This type of scattering process was first associated with the detection of grating structures in crystalline media, which gave William Lawrence and William Henry Bragg a Nobel Prize in 1915. But the scattering principles are universal as illustrated in Fig. 4.3.1:

For an incoming wave at wavelength λ_s that is affected by a structure with irregularities repeated at distances λ_s but extended in the perpendicular direction, then the backscattered signals at an angle θ from the individual scatters are all in phase if the Bragg condition is fulfilled:

$$n\,\lambda_r = 2\,\lambda_s \sin\theta \qquad (4.3.1)$$

where n is an integer. It should be noted that the incoming wave must arrive in directions perpendicular to the elongation of the structure (i.e., the rays are in the paper plane in Fig. 4.3.1).

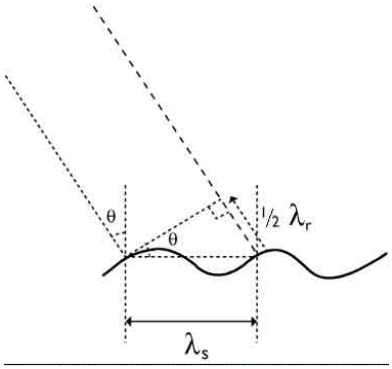

Figure 4.3.1. Bragg scatter principle.

In an ionized medium like the ionosphere there exist a vast number of plasma waves and their physics is a complicated issue for which specialized literature should be consulted. Hence only a few general remarks shall be added.

Wave-like ionospheric structures can be generated within the ionosphere by plasma instability processes, for instance, by strong electric fields that make the electrons move fast relative to the ions in regions (notably the E-region) where the collisions tend to stop the ion motion (two-stream instability), or by strong density gradients (gradient-drift instability) in drifting ionosphere regions (E- and F- regions). But such structures could also be impressed from outside conditions like turbulence in the upper atmosphere associated with tides and gravity waves in the lower ionosphere regions (D- and E-regions) or by impinging large-scale waves or modulated electron precipitation initially generated in the magnetosphere. It should be mentioned that the coupled thermal motion of electrons and ions can be resolved into a spectrum of ion-acoustic plasma waves.

The effects from such wave-like structures on propagating radio waves are largest when the rays enter perpendicular to the elongation direction and satisfy the Bragg conditions. In the D-region the layering of irregularities is essentially controlled by the neutral atmosphere and thus horizontally elongated. In contrast, the kilometer-to-centimeter sized irregularities in the E- and F-regions are predominantly elongated along the direction of the Earths magnetic field. At wavelength scales comparable to the Debye length the ion-acoustic waves representing the thermal motions are more or less randomly oriented.

Differential drift of electrons and ions (i.e., electric currents) and gradients are caused by different mechanisms in the equatorial, mid-latitude, and auroral regions. In the equatorial regions tidal winds create polarization electric fields that generate the equatorial electrojet in which instabilities grow. In mid-latitude regions wind shear due to gravity waves and tides may create sporadic E-layers characterized by strong electron density gradients, which in turn result in instabilities.

In the auroral regions electric fields generated in the magnetosphere are impressed on the ionosphere and cause strong **E** x **B** drifts, which in the upper (collisionless) ionosphere give the same motion for electrons and the heavier ions. In the lower ionosphere the ion motion is stopped first by their collisions with neutral

atmospheric constituents while the electrons continue their drift, which result in electric currents in directions opposite of the drift. If the differential drift velocity exceeds the ion-acoustic wave velocity then the two-stream plasma instability may be exited and generate electron density structures that are elongated in the direction of the magnetic field and propagate approximately in the direction of the electron drift. Energetic electron precipitation from the magnetosphere that may cause visual auroras can generate steep electron density gradients, which in turn give rise to plasma instabilities that generate wave-like irregularity structures.

These scatter processes give rise to a host of radio wave phenomena. For ionosonde or digisonde observations they cause backscatter reflections that may give additional traces from sporadic layers (e.g., Ess) or massive spread reflections over wide height and frequency ranges (e.g., spread-F) that in turn may blur large sections of the ionograms. For coherent scatter techniques like that used in the STARE or Super DARN radar systems the ionospheric scatter of the radar signals is a prerequisite for the measurements. For these observations the transmitted rays need to enter perpendicular to the magnetic field direction to fulfil the backscatter conditions. For the "incoherent" radars (which are not quite incoherent), the major backscatter process is the coherent Bragg-scattering from ion-acoustic structures generated by the thermal motions.

For signals propagated through ionospheric regions with scatter activity the amplitudes and phases of the received waves may fluctuate strongly, which give rise to so-called scintillations in the received signal as illustrated in Fig. 4.3.2.

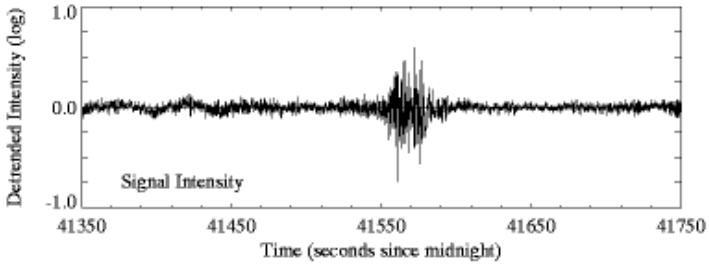

Figure 4.3.2. Scintillations in received signal intensity. From NWRA web site. http://www.nwra.com/ionoscint/sp_intro.html

For transmission of communication signals to and from satellites or for GPS transmissions these scintillations are most severe when the signals pass through the ionosphere near equator or in the auroral and polar regions. Fig. 4.3.3 presents an illustrative example of the global occurrences of scintillations at a specific UT time. Fig. 4.3.4 presents an example of simultaneous scintillation and total electron content (TEC) measurements.

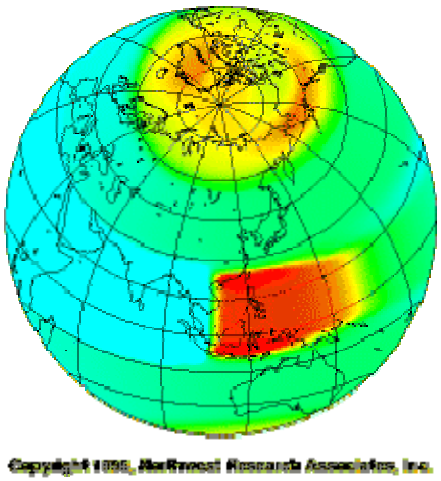

Figure 4.3.3. Global occurrences of scintillations.(From NWRA web site)

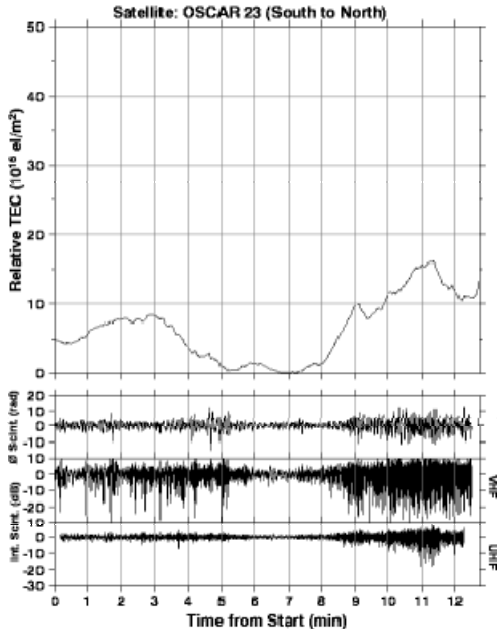

Figure 4.3.4. Scintillations and total electron content From NWRA web site.

Links and further readings:

Northwest Research Associates (NWRA): http://www.nwra.com/ionoscint/sp_intro.html
Scintillation levels at solar max: http://www.nwra.com/ionoscint/sp_solmax.html
NWRA real-time data: http://www.nwra.com/ionoscint/sp_rtdata.html

References:

Buneman O.(1963), Excitation of field aligned sound waves by electron streams, Phys. Rev. Lett., 10, 285, 1963.
del Pozo, C. F., J. C. Foster, and J.-P. St. Maurice (1993), Dual-Mode E Region Plasma Wave observations from Millstone Hill, J. Geophys. Res., 98, 6013-6032, 1993.
Farley D. T. (1963), A plasma instability resulting in field aligned irregularities in the ionosphere, J. Geophys. Res., 68, 6083, 1963.
Fejer, B. G. and M. C. Kelley (1980), Ionospheric Irregularities, Rev. Geophys. Space Phys., vol 18, 401-454.

Reference books:

Davies, K. (1990, 2008), Ionospheric Radio, First Edition: 1990, Peregrinus Ltd., Reprinted: 2008, The Institution of Engineering and Technology, London.
Hargreaves, J. K. (1992), The Solar-Terrestrial Environment, Cambridge University Press.
Levis, C. A., J. T. Johnson, and F. L. Teixeira, Radiowave Propagation: Physics and Applications, John Wiley & Sons, Inc., 2010.

5. Instrumentation for Ionospheric observations.

A vast number of instruments and methods have been invented and employed to remotely examine the ionosphere by examination of signals affected by the ionized medium. The measuring techniques could be divided according to the type of interaction between wave fields and the medium in three groups:

i. Coherent interaction where all charged particles respond the same way to wave field.
ii. Scatter interaction where the charged particles are organized in structures that interact with the wave.
iii. Incoherent scatter where the individual particles scatter or backscatter the wave field.

A short and far from complete list of instrumentations is given here:

i. Ionosondes (coherent refraction and reflections; occasional scatter)
ii. Digisondes (coherent refraction and reflections; occasional scatter)
iii. GPS transmission receivers (coherent refraction; occasional scintillations)
iv. Riometers (coherent absorption, occasional scintillations)
iv. Coherent scatter radars (scatter reflections; refraction of rays)
v. Incoherent scatter radars (incoherent scatter, occasional coherent scatter)

5.1. Ionosondes. The ionosonde is essentially a swept frequency radar that measures the elapsed time between the transmission of continuous wave (CW) pulses and the reception of their reflections from the ionosphere. Assuming propagation at the speed of light, c, the delay, Δt, measures the virtual (apparent) height of the reflecting layer: $h' = 0.5c\Delta t$. The real height is lower since the true signal (group) velocity is always lower than c.

Typically, the operating frequency is varied between a few hundred kHz and 20 Mhz during a sweep lasting 2-5 min. The pulse duration is 30 μs and repetition frequency is 50 pps. Output power is 10 kW. The antenna is a vertical delta antenna used both for transmitting and receiving. The received signal reflected from the ionosphere can be seen at an oscilloscope connected to the receiver output and synchronized to the transmitting pulse (A-scan). The signal can be used to blank the trace (B-scan). If the screen is photographed on a slowly moving film then a ionogram picture is formed in the course of the frequency sweep. The trace from a pulse corresponds to a vertical line in the ionogram. The base-line (0 km) mark the transmission. Marker (blanking) lines are usually inserted to scale the operating frequency and the delay time (virtual height). The ionograms need careful (time-consuming, delaying) manual scaling.

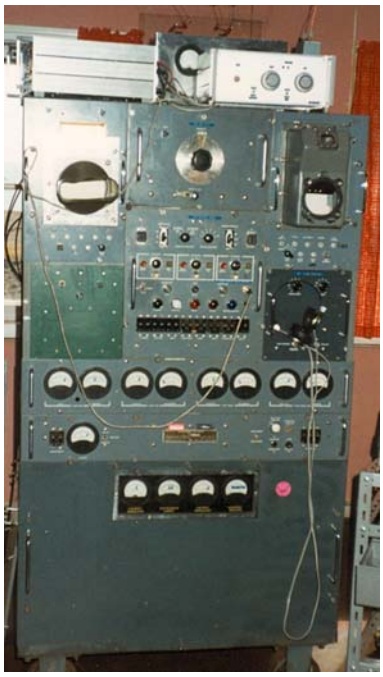

Figure 5.1.1. An old (C4) ionosonde (Narsarsuaq, Greenland). Photo: DMI.

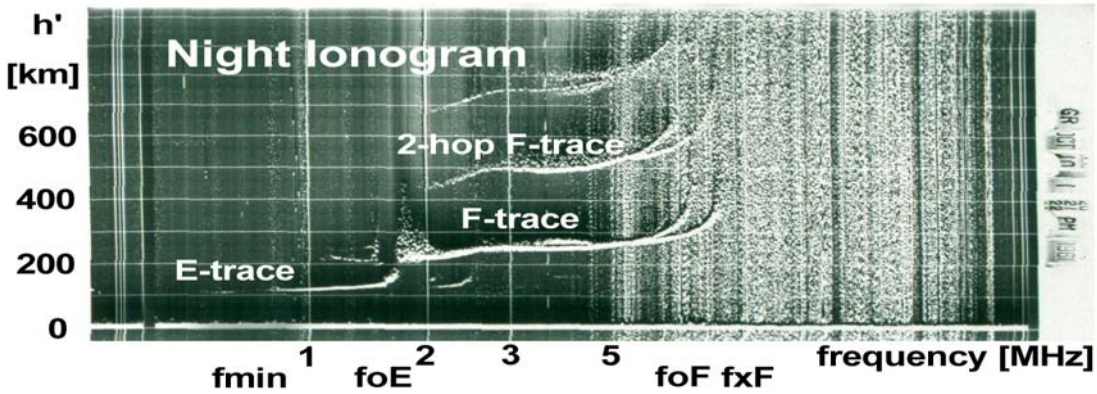

Figure 5.1.2. Typical night ionogram. Simple E- and F-layer structure. Multiple hop indicate low absorption.

5.2. Digisondes. Now, most (analog) ionosondes have been replaced by digisondes. The operating principle of a digisonde resembles that of the ionosonde. A widely used instrument is the University of Lowell "Digisonde Portable Sounder" (DPS), capable of making measurements of the overhead ionosphere and providing real-time on-site processing and analyses to characterize radio signal propagation to support communications or surveillance operations.

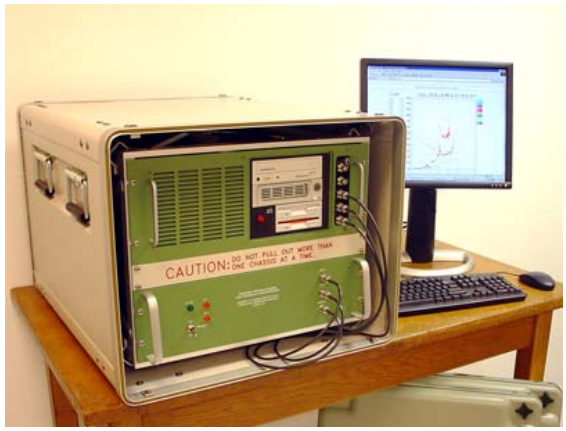

Figur 5.2.1. University of Lowell Digisonde.

The system compensates for the low transmitter power (300 W vs. 10 kW for previous systems) by employing intrapulse phase coding, digital pulse compression and Doppler integration. The data acquisition, control, signal processing, display, storage and automatic data analysis functions have been condensed into a single multi-tasking, multiple processor computer system, while the analog circuitry has been condensed and simplified by the use of reduced transmitter power, wide bandwidth devices, and commercially available PC expansion boards. The DPS integrated transceiver package and display unit is shown in Fig.5.2.1. The transmitter antenna could be simple, for instance, a vertical delta antenna. The receiving system uses four crossed magnetic dipole receiving antennas mounted in a specific pattern shown in Fig. 5.2.2.

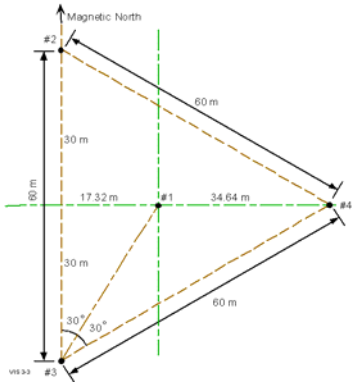

Figure 5.2.2. Digisonde antenna array.

With this antenna layout and special data processing routines, the DPS forms seven beams, one overhead (0° zenith angle) and six oblique beams (the nominal 30° zenith angle can be changed by the operator) centred at North and South directions and each 60° in between. Using the same four complex samples (at one reflection height at a time) seven overlapping beams are formed, one overhead (for which the phase shifting required on each antenna is 0°) and six beams each separated by 60° in azimuth and tipped 30° from vertical. If one of the off-vertical beams is found to produce the largest amplitude, the displayed echo on the ionogram is color coded as an oblique reception.

The University of Lowell Digisonde instrument performs simultaneous measurement of seven observable parameters of reflected (or in oblique incidence, refracted) signals received from the ionosphere:

1) Frequency
2) Range (or height for vertical incidence)
3) Amplitude
4) Phase
5) Doppler Shift and Spread
6) Angle of Arrival
7) Wave Polarization

Fig. 5.2.3. displays an example of an ionogram taken by this DPS (from ulcar.uml.edu).

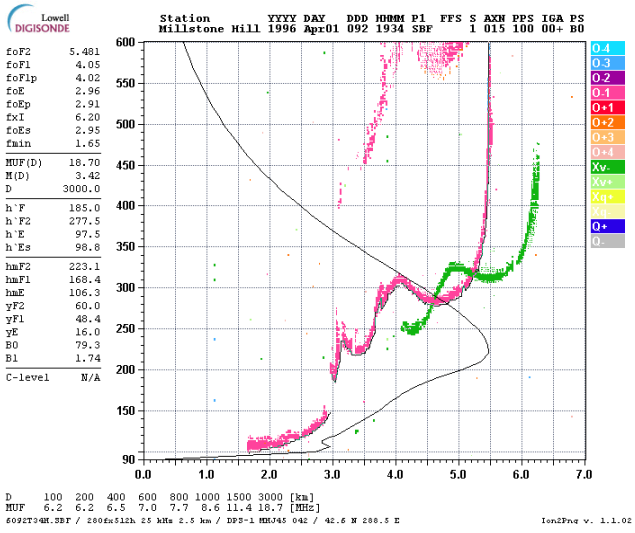

Figure 5.2.3. Ionogram taken by Univ. Lowell Digisonde.

The physical parameters of the ionospheric plasma affect the way radio waves are reflected from or pass through the ionosphere. Thus, it is possible by measuring all of these observable parameters at a number of discrete heights and discrete frequencies to map out and characterize the structure of the plasma in the ionosphere. Both the height and frequency dimensions of this measurement require hundreds of individual measurements to approximate the underlying continuous functions. The resulting measurement provides an ionogram and comprises a seven-dimensional measurement of signal amplitude vs. frequency and vs. height. Due to the limitations of the software only five may be displayed at a time. Fig. 5.2.3. is a five-dimensional display, with sounding frequency as the abscissa, virtual reflection height (simple conversion of time delay to range assuming propagation at $c=3x10^8$ m/sec) as the ordinate, signal amplitude as the spot (or pixel) intensity, Doppler shift as the colour shade and wave polarization as the colour group (the blue-green-grey scale or "cool" colours showing extraordinary polarization, the red-yellow-white scale or "hot" colours showing ordinary polarization).

In the ionogram displayed in Fig. 5.2.3. the traces are colour-coded to mark the polarization of the received signal. Here, the trace for the reflected “ordinary” (“O”) characteristic wave is marked in red while the trace for the reflected “extraordinary” (“X”) characteristic wave is marked in green. Starting from the lowermost altitudes and the lowest frequencies and focusing on the O-trace, there is a trace for the E-layer ranging up to the “critical frequency” of 3.0 MHz. The critical frequency for a layer, where the virtual height has an asymptotic trend, corresponds to a local maximum in electron density. The reflections between 3.0 and 4.0 MHz comes from the F1 region. First the virtual height is decreasing from its asymptotic behaviour and then the virtual height increases again indicating an increased steepness of the electron density profile, but no local maximum. From 4.0 to 5.5 MHz the reflections come from the F2 region. The F2 region electron density peak gives the asymptotic increase of the virtual height at 5.5 MHz.

With an almost complete trace (extracted as the thin black line tracking the reflections) extending up from the lowest frequencies it is possible to invert the virtual heights to produce real heights corresponding to the reflections up to the maximum critical frequency (F2 peak). The deduced real height profile is displayed in the thin black line. The extension above the F2-layer peak is a modelled extrapolation not provided for in the ionogram data. The displayed reflection frequencies can be converted into electron densities by using the reflection condition $X = \omega_p^2/\omega^2 = 1$. Inserting the constants used to define the plasma frequency, ω_p, gives:

$$N_e = f^2 / 80.5 \text{ [electrons/m}^3 \text{ when f is in Hz]} \qquad (5.2.1)$$

thus, in the present case, the E-region maximum electron density is $1.1\ 10^5$ [electron m^{-3}] while the F2 peak density is $3.8\ 10^5$ [electrons m^{-3}].

The extraordinary (X) characteristic wave is subjected to stronger frequency-dependent damping in the ionospheric D-region. Hence the lower part of the X-trace does not extend to as low frequencies as the O-trace. The upper part of the X-trace is shifted by an amount equal to around half the local electron gyro frequency since the reflection condition is now $X = \omega_p^2/\omega^2 = 1 - Y = 1 - \omega_b/\omega$. Thus for $\omega_p >> \omega_b$

$$f(\text{reflection}) = 0.5\ f_b + (0.25\ f_b^2 + f_p^2)^{½} \sim f_p + 0.5\ f_b \qquad (5.2.2)$$

The electron gyro frequency, f_b, is around 1.5 MHz. Hence for the F-region (f_p ~5.5 MHz) the approximation is valid within ~2%.

The left part of the image in Fig. 5.2.3. presents ionogram scaling results, which primarily comprise the critical frequencies and the virtual and real heights for the regular ionospheric layers. An additional derived parameter is the so-called Maximum Usable Frequency (MUF) for different distances ranging from 100 to 3000 km. The MUF represents the highest frequency that could be propagated between two sites by a radio signal via a single hop transmission with ionospheric reflection considering the actual ionospheric profile and taking into account the curvature of the Earth.

The “nice” ionogram presented in Fig. 5.2.3. is typical for daytime at mid-latitudes and for undisturbed conditions. During night the E-region electron densities are markedly reduced and the F1 region trace may completely disappear. Hence the ionogram may show only a reduced E-region (much lower critical frequency) and a single F-region trace (c.f. Fig. 5.1.2.) giving an even simpler appearance.

Usually, the ionograms taken in other than mid-latitude regions or during disturbed conditions could be quite different and the interpretation of the complicated traces would be much more demanding. The reflection traces from the regular ionospheric layers could be much disturbed and in addition entirely different traces based on scatter reflections from wave-like ionospheric irregularities may appear. Very comprehensive reviews of ionograms from different sites and various conditions are provided in UAG Reports no. 23, “URSI Handbook on Ionogram Interpretation and Reduction”, and no. 50 “High Latitude Supplement”. Here, only a few examples of diversion from regular ionospheric behaviour shall be discussed.

Sporadic layers. Additional ionization may be produced by various processes, among other, precipitation of energetic electrons during auroral substorm events. During such events that are most frequent in the night side of the auroral regions intense showers of energetic particles, primarily electrons and protons, may enter the upper atmosphere. One of the consequences is the formation of strongly enhanced E-layers at altitudes of around 100-150 km. Such layers may enhance the signal strength for short-range transmissions but could be too variable to provide adequate signal quality. At the same time the propagation via F-region layers at higher altitudes could be disabled by the shielding (“blanketing”) effects of the dense E-region, which could have critical frequencies (i.e., electron densities) in excess of those of the F-region. In consequence the long-distance transmissions which rely on the high altitude of the ionospheric “mirror” might suffer. In most cases, however, the sporadic E-layers are partly transparent such that signals can pass through to reach F-region altitudes.

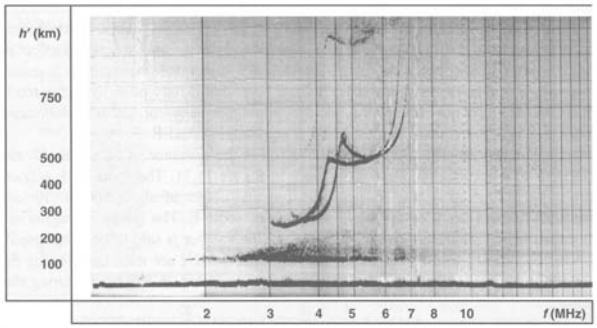

Figure 5.2.4. Ionogram with tranparent sporadic E-layer. (From Concright, NGDC. In: Levis et al., 2010, p.256)

F-region depressions. During magnetic storms the F-region electron densities may dramatically decrease due to processes that either increase the recombination efficiencies or removes the ionization by enhanced horizontal or vertical drift. The result is a lowering of F-region critical frequencies and, therefore, a lowering of the maximum usable frequencies. Since the best signal strength and quality is usually obtained at the higher frequencies where the D-region absorption is smaller, such lowering of the operating frequency range may deteriorate the transmissions. At high latitudes, magnetic storm conditions are often accompanied by events of increased absorption. Hence the minimum useable frequency could be substantially increased, which would make the frequency window shrink from the low-frequency end. In addition, the multiple services in the HF range are more prone to disturb each other since they have to operate within a more narrow range of frequencies.

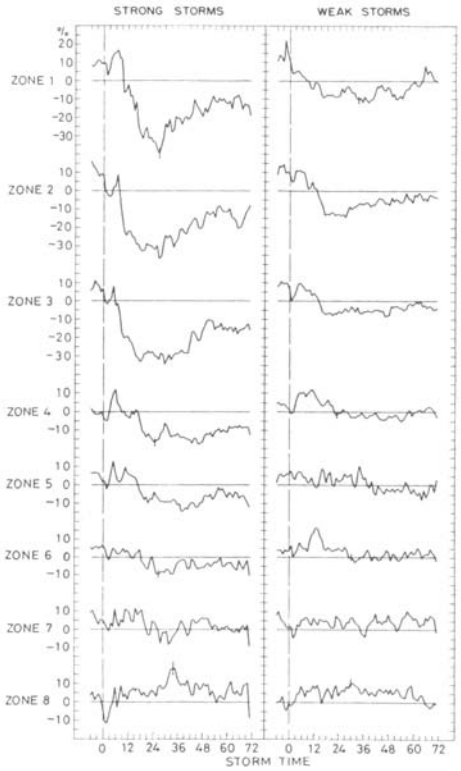

Figure 5.2.5. Storm depression of F-region critical frequencies. From Matsuhita, 1969. In: Davies 1990, p.339

Fading and flutter. The conditions for ionospheric propagation of radio waves may change rapidly during various disturbances where ionospheric densities or layer heights vary. One example is variations in the shape of the reflecting layer from plane to convex or concave. Such changes may cause the transmitted ray to be more or less focused with the result that the received signal varies considerably in strength. In another example the location of the reflection site for the transmitted ray may shift around such that the phase path for the signal changes all the time. Such changes may imply Doppler shifts in the received signal which could blur the transmission and even take the signal out of the allocated frequency band. Further examples imply changes in the electron densities and thus in the refractive index along the signal path. Such changes may cause phase and amplitude changes in the received signal, which may strongly deteriorate the transmission quality. The list of possible reasons for fast (flutter) or slow fading of signals transmitted via the ionosphere is quite extensive.

Scatter. As discussed above, various plasma processes may generate wave-like structures in the ionosphere. Such disturbances are in particular frequent at conditions that produce large ionospheric electric fields and currents related, for instance, to the auroral or equatorial electrojets. In the ionograms such conditions produce scattered return signal, backscatter, which may blur the regular reflections. A few services use forward scatter in their transmission techniques. However, for most radio transmission services such scatter processes usually disturb the signals both by scattering power out of the transmitted radio signals and also by adding unwanted spurious contributions in and out of phase with the main signal to produce scintillations in the strength and phase of the received signal. An example of scatter in an ionogram is displayed in Fig. 5.2.6.

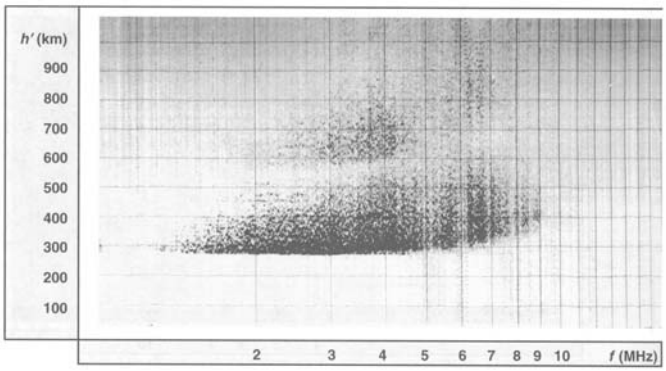

Figure 5.2.6. Ionogram with Spread-F backscatter. (From Concright, NGDC. In: Levis et al., 2010, p.256)

5.3. GPS receivers for Total Electron Content (TEC) measurements.

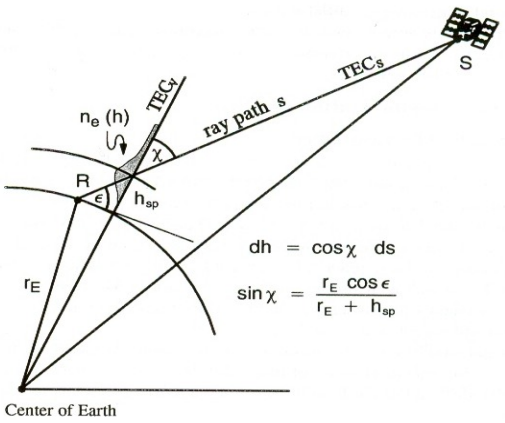

Figure 5.3.1. Satellite-ground transmissions. From Jacowski, 1996 (in Kohl,1996,p373)

The ionospheric influence on radio signals can be described in terms of the refractive index, which differs from unity and, therefore, causes changes in amplitude, phase, polarization and ray path of radio waves propagating through the medium. The corresponding effects on navigation signals comprise signal code propagation delays and advancements of signal carrier phase. These effects, while degrading the accuracy of navigation signals, can however be used in the diagnostics of the ionosphere particularly in dual frequency (or dual polarization) measurements between a spacecraft and a ground station.

Measurements of the differential carrier and modulation phases have proven a useful way of getting information about the total columnar electron content of the ionosphere since the early days of satellite launches. A few satellites, for instance ATS-6, have been equipped with radio beacon experiments while in other cases, for instance the satellites used in the Global Positioning System (GPS), the ionospheric probing has been a bi-product of signal transmissions for other purposes.

The GPS satellites transmit two coherent frequencies in the L-band, at L1 with f1=1575.42 MHz and L2 with f2=1227.60 MHz. The L1 frequency is modulated by a public Coarse/Acquisition (C/A) code with an effective modulation frequency of around 1 MHz (wavelength~300m). Both carrier frequencies are modulated by a precise (P or Y) code with an effective modulation frequency of around 10 MHz (wavelength~30m). The signal path through the ionosphere from the satellite to ground is sketched in Fig. 5.3.1.

Generally, the phase φ (in cycles) of the received signal can be written in terms of an integral of the refractive index, μ, along the signal path as:

$$\varphi = f\,(t - (1/c) \int \mu \, ds) \qquad (5.3.1)$$

where the refractive index, in a high-frequency approximation ($\omega >> \omega_p$, collisions and magnetic field neglected) with $\omega_p^2 = N_e q^2/\varepsilon_0 m_e$, and the dimensionless quantity $X = \omega_p^2/\omega^2$, can be written:

$$\mu = (1-X)^{1/2} \sim 1 - 0.5\,X = 1 - K\,N_e/f^2 \;, \quad K = 40.3\ [m^3/s^2] \qquad (5.3.2)$$

The L1 and L2 GPS frequencies f1 and f2 are both derived from a common fundamental frequency $f_0 = f_1/m_1 = f_2/m_2$. Reducing in the receiver both signals to the common frequency, then the phase difference in terms of cycles of f_0 between the L1 and the L2 carrier signals is:

$$\Delta\Phi = \Phi_1 - \Phi_2 = K\,(f_0/c)\,(1/f_1^2 - 1/f_2^2)\,TEC \;, \quad TEC = \int N_e \, ds \quad [electrons/m^2] \qquad (5.3.3)$$

or in terms of an equivalent difference, d_I,' in path lengths:

$$d_I' = K\,(1/f_1^2 - 1/f_2^2)\,TEC \qquad (5.3.4)$$

where TEC is the total electron density integral along the signal path. However, the carrier cycles are not marked individually; hence, there is an ambiguity in the phases of both carriers corresponding to integer numbers N1 and N2 of wavelengths λ1 and λ2. Hence the true difference in path lengths is:

$$d_I = K\,(1/f_1^2 - 1/f_2^2)\,TEC + \lambda_1 N_1 - \lambda_2 N_2 \qquad (5.3.5)$$

The modulation signals (C/A, P or Y code) transmitted with the L1 and L2 carriers propagate with the group refractive index μ_g , which in the high frequency approximation can be written:

$$\mu_g = 1/\mu = 1/(1-X)^{1/2} \sim 1 + 0.5\,X = 1 + K\,N_e/f^2 \;, \quad K = 40.3\ [m^3/s^2] \qquad (5.3.6)$$

For a common modulation signal of frequency f_m the calculations gives for the phase difference:

$$\Delta\Phi_m = \Phi_{m2} - \Phi_{m1} = K\,f_m/c\,(1/f_1^2 - 1/f_2^2)\,TEC \qquad (5.3.7)$$

For GPS signals the modulation signals hold various information. The ranges determined from the code phases are called pseudo-ranges. Considering only the L1 GPS frequency modulated by the C/A code the ionospheric range addition (error for navigation services) is directly proportional to TEC and amounts to:

$$d_I = 1.62\ 10^{-17}\ TEC \qquad (5.3.8)$$

which for typical TEC values gives values of several meters.

The ionospheric contribution to the difference in pseudo ranges between L1 and L2 signals is:

$$\Delta p_I = p_2 - p_1 = K\,(1/f_1^2 - 1/f_2^2)\,TEC \qquad (5.3.9)$$

Thus, measurements of the phase difference between the code modulation signals on the two carriers can be used to derive TEC values for the actual path from the each of the satellites to each of the ground receiving stations. These oblique TEC values are then processed and converted to a global 4-D distribution of electron densities from which vertical maps of time-varying TEC as well as electron density slices can be extracted.

The present global array of ground-based GPS receivers is shown in the map in Fig. 5.3.2. In the map is also indicated the range of positions (marked by a circle) within which signals from a GPS satellite can be safely received. Fig. 5.3.3. presents an illustrative example of a TEC map based on GPS data only.

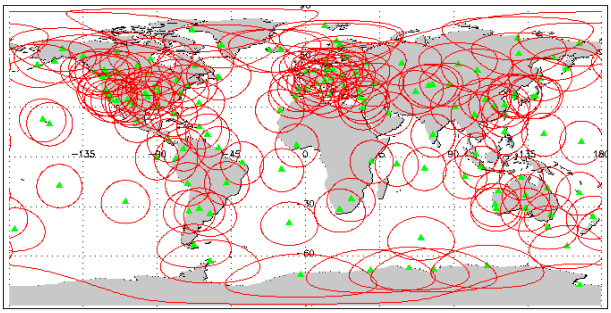

Figure 5.3.2. Global array of GPS receiving stations. (GAIM project: http://iono.jpl.nasa.gov/gaim/intro.html)

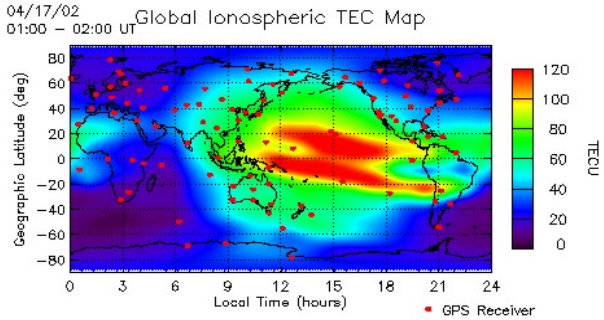

Figure 5.3.3. Global map of ionospheric TEC. (GAIM)

Fig. 5.3.4. presents an example of the TEC data acquired by the "Global Assimilative Ionospheric Model" (GAIM) operated by JPL and USC. GAIM includes additional data, for instance, from the digisonde network but the GPS line-of-sight data form the basis for the TEC maps.

The vertical TEC results have in many cases been compared to electron density values obtained by different more localized techniques, for instance, by incoherent scatter radar measurements of the total vertical electron density profiles. Generally, good agreement has been found.

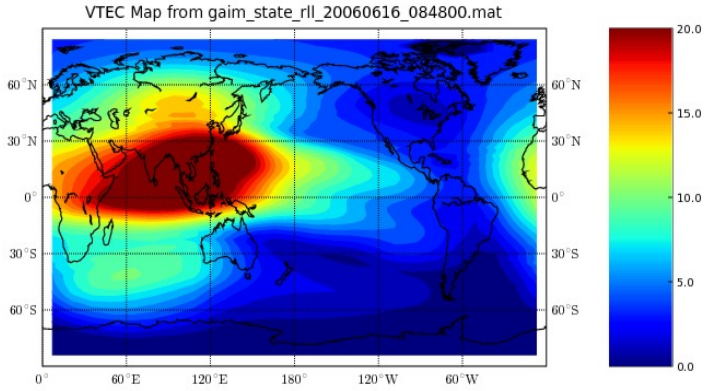

Figure 5.3.4. Example of real-time TEC map. (GAIM project)

5.4. Riometers.

A RIOmeter (Relative Ionospheric Opacity - meter) is, in principle, a sensitive, calibrated radio receiver which measures the signal strength of the weak signals received from sources in the sky. Most often a vertical antenna is being used for single-beam riometer observations. The measuring frequency is normally in the HF-VHF frequency range, typically around 30 MHz.

The signals are radio noise (cosmic noise) generated by stars and galaxies. These signals are virtually invariant in time so the source strength depends only on the look direction into space. On their path to the receiving antenna the signals pass through the upper ionized atmosphere, the ionosphere. The radio wave

absorption intensity depends on the number density of free electrons as well as the frequency of collisions between electrons and the heavy constituents.

The antenna scans the same strip of the sky every sidereal day (shorter than the UT day by 4 min). Thus the relative absorption of the cosmic noise is calculated by determining the departure of the actual signal from the signal level recorded at the same sidereal time during a quiet day without ionospheric absorption. The undisturbed signal level recorded during a sidereal day is called the Quiet Day Curve (QDC).

By recording the varying signal strength of the received cosmic noise and thus observing the ionospheric absorption one may determine the combined effects of changes in the electron densities and in their collision frequencies. Such changes may occur as the result of solar flare activity or geomagnetic storm and substorm processes. These disturbance events may generate radiation of high-energy electrons and ions, notably protons. Precipitation of the energetic radiation into the upper atmosphere creates additional ionization, typically at 60-100 km of altitude. The electron collision frequencies are high at these altitudes. Consequently, the absorption of radio waves passing through this region will be enhanced.

Such events of precipitation of energetic particles and absorption (black-out) of radio waves in the upper atmosphere in association with solar flares and geomagnetic storms are particularly frequent and intense in the auroral and polar regions. The riometer observations from an extended net of stations are particularly well suited to explore the large-scale temporal and geographical development of such events.

The riometer technique was developed for the International Geophysical Year by C. G. Little. A simplified diagram is presented in Fig. 5.4.1. The receiver is switched between the antenna and a steerable noise source adjusted to balance the antenna signal. The control voltage proportional to the noise power provided by the noise generator is recorded. The antenna systems used then were usually simple Yagi (e.g. 3-element) or a double dipole structures.

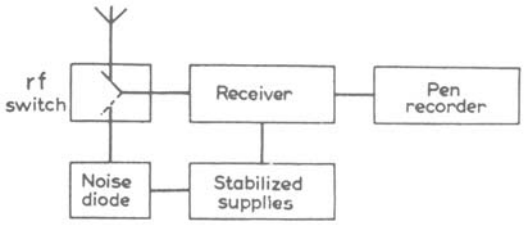

Figure 5.4.1. Simplified riometer block diagram. (From C.G. Little, 1957)

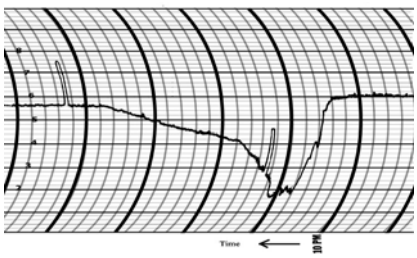

Figure 5.4.2. Riometer chart recording

An early example of a riometer chart recording for one hour is shown in Fig. 5.4.2. (http://www.lajollasciences.com) Note that the time is running from right to left. The recorded level is probably close to the QDC at the start and end of the recorded interval. For the recorded event the level suddenly changes from 0.6 of full scale to 0.2, thus the absorption is 10 $\log_{10}(0.6/0.2)$ = 4.8 dB.

Basically, the riometer systems presently at work uses the same principles. Fig. 5.4.3. displays a block diagram of a modern LaJolla riometer. The instrument has been manufactured for almost 40 years in continually updated versions. Fig. 5.4.4. displays the antenna system with 4 crossed Yagi antennas used for single-beam riometer observations at the HAARP research facility in Alaska.

The riometer data from the HAARP installation are available on-line in real time from the link: (http://www.haarp.alaska.edu/haarp/data.htm). An example of these data is shown in Fig. 5.4.5. The diagram presents the riometer recordings for an interval of 1.5 days.

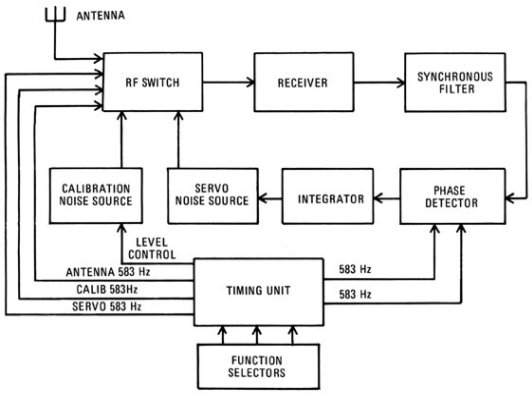

Figure 5.4.3. LaJolla Riometer diagram.

The riometer data are displayed in blue line. The quiet level (QDC) has been added in green line. The difference between the two curves marks the absorption intensity and is usually scaled in dB. The scaled absorption values are displayed in red line. Note the series of typical auroral absorption events up to around 2 dB occurring at the end of the display.

Figure 5.4.6. displays the on-line real-time data from 3 consequtive days. Again, the riometer data are displayed in blue line and the QDC in green. Note the series of auroral absorption events recorded on the last day (10 Oct 2010) of the recorded interval. At other times (mostly around local noon) the recordings are disturbed by interference that generates spiky positive (upward) deflections.

Figure 5.4.4. 4-Yagi HAARP riometer antenna system. Photo from HAARP web site.

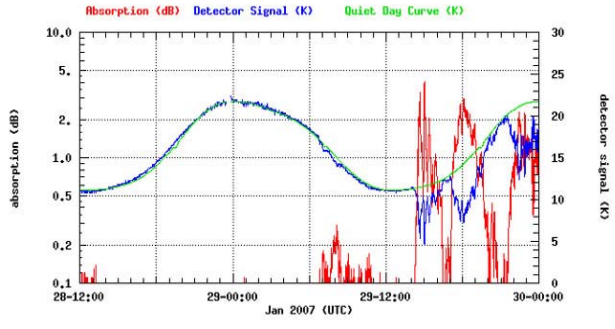

Figure 5.4.5. Example of HAARP riometer data. Riometer. in blue, QDC in green, Absorption. in red. From HAARP web site.

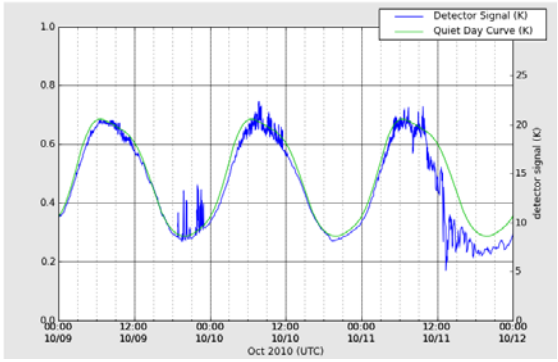

Figure 5.4.6. Real-time HAARP riometer recordings (on-line). Riometer in blue, QDC in green line. From HAARP web site.

In addition to single-beam riometers, various types of multi-beam riometer instrumentations have been operated. A widely used type is the “Imaging Riometer for Ionospheric Studies” (IRIS) which, in principle, comprises a set of highly sensitive, calibrated radio receivers (riometers) that measure the signal strength of the weak radio signals received from various directions of the sky. Usually the IRIS riometer system uses an array of antenna elements (e.g. dipoles) which are combined through a so-called "Butler Matrix" to form a number of regularly spaced narrow beams. Typical antenna systems comprise 49 or 64 beams distributed in a regular pattern over a field of view extending within 45 degrees from vertical. The measuring frequency will be in the HF-VHF range, typically at 38 MHZ within the protected frequency band reserved for radio astronomy.

The imaging riometer system measures the time-varying absorption intensities in many different directions simultaneously. From these data one may derive sequences of images of the instantaneous absorption intensity distributions. Typically, the imaging riometer technique provides observations with a time resolution of around 1 sec of the dynamic absorption intensity distribution over an area of typically 250 x 250 km referred to an ionospheric level of 90 km. The first IRIS instrument was developed at Univ. Maryland in a 49-beam version and installed at South Pole station by T. J. Rosenberg and D. Detrick in 1988. Now, more than 20 imaging riometers of constructions with 16 to 256 beams are in operation worldwide. This instrumentation is particularly well suited to observe the very dynamic and often strongly localized occurrences of auroral absorption events.

Absorption events observable using riometer techniques may be divided into categories according to the main responsible cause. During undisturbed conditions the cosmic noise signals penetrating from space to the ground are exposed to a weak, slowly varying absorption which largely depends on the ionization in the upper atmosphere produced by the normal solar ultra-violet radiation. At disturbed conditions the enhanced emission of solar UV- and X-rays during the active phases of flares cause sudden cosmic noise absorption (SCNA) events all over the day-side of the Earth. During the larger flares the sun may also emit an intense radiation of high-energy particles, notably electrons, protons, and α-particles. When these particles arrive at the Earth they may precipitate into the atmosphere over the polar regions to produce polar cap absorption (PCA). In most cases protons with energies of the order of 1 to 100 MeV are the dominant cause of PCA events. The high energy (.1 - 10 MeV) solar electrons may, however, be important in some events particularly during the initial phases.

During magnetospheric substorm activity, cosmic noise absorption events of various types are observed in the different local time sectors of the auroral zones. These events are mostly caused by the precipitation of energetic substorm electrons which may considerably enhance the ionization in the D- and E-regions. The particle spectra are generally softer at local night where the absorption typically relate to the precipitation of 10 - 100 keV electrons. In the morning and day sectors the particle spectra tend to be harder and cosmic noise absorption events are now typically related to the precipitation of 30 - 300 keV electrons.

Fig. 5.4.7. displays examples of riometer data recorded during a major solar flare event. In the figure the fields are ordered with data from the highest (polar) latitudes on top down to auroral zone latitudes at the bottom. Sondrestrom at the middle of the diagram is situated at around 75° geomagnetic latitude. The black triangles above the fields mark the occurrences of major solar flares. It is seen that the absorption intensities increase at all latitudes forming a Polar Cap Absorption (PCA) event just after the flare events as the result of the intense radiation of high-energy solar protons, typically 10 – 100 MeV the may reach the lower part of the ionospheric D-region down to altitudes around 60-90 km. An empirical relation between riometer absorption L (in dB) on 30 MHz and the omnidirectional, greater than 20 MeV proton flux F (in protons cm^{-2} s^{-1}) is (Davies (2008), p.328):

$$L = \int \text{const.}\ N\,\nu / \omega^2\, ds \ \sim\ 0.13\, F^{1/2} \qquad (5.4.1)$$

Thus, for an intense PCA event with L > 20 dB, the flux of solar protons above 20 MeV is F > 20 000 protons cm^{-2} s^{-1}.

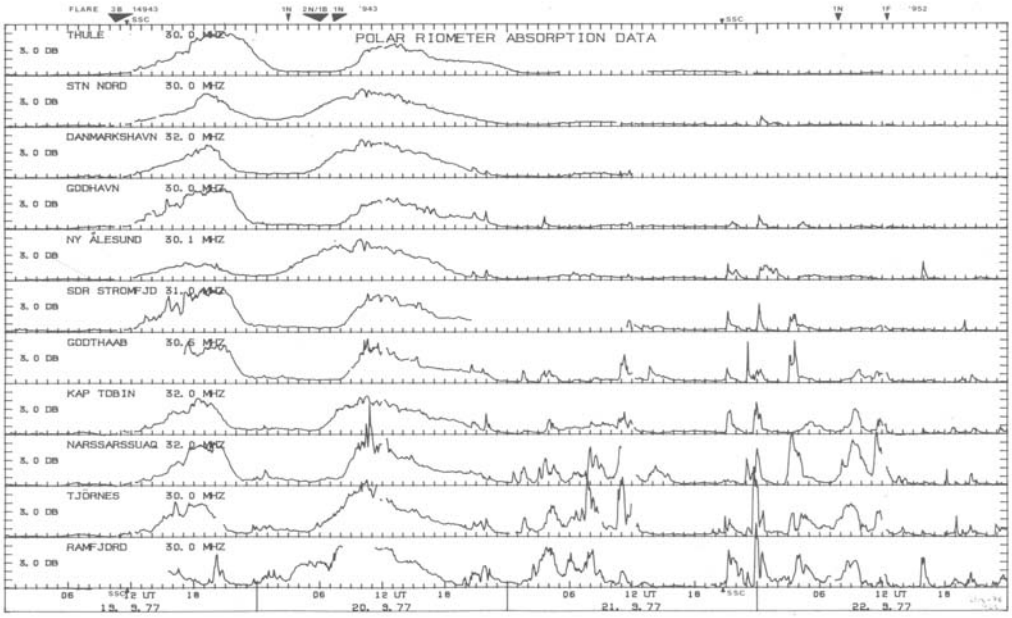

Figure 5.4.7. Polar Cap Absorption (PCA) and Auroral Absorption (AA) events. (Stauning, 1978)

Furthermore, Fig. 5.4.7. indicates that as the relatively smooth PCA event weakens after 2 days then the data from stations near the auroral zone display spiky absorption events typical of Auroral Absorption (AA) occurrences. Such AA events are part of the general substorm-related disturbance spectrum. They are caused by precipitation of high-energy electrons, typically of energies in the range 10-100 keV that may reach the lower E- and upper D-regions at altitudes of around 90-120 km.

Such auroral absorption events could be studied in greater details by imaging riometers. Fig. 5.4.8. displays the multiple antenna beam patterns for the IRIS installation at Kilpisjärvi in Northern Finland.

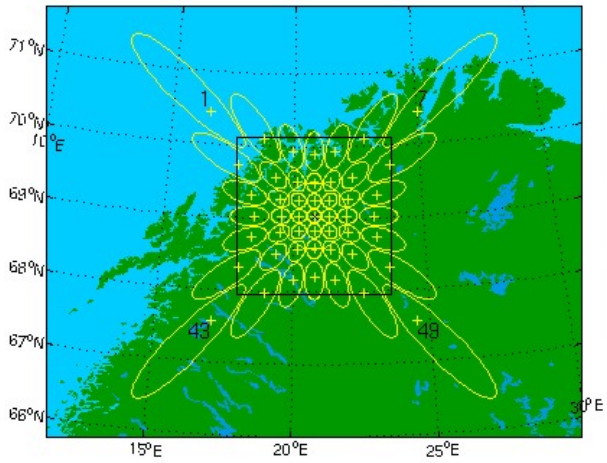

Figure 5.4.8. IRIS-Kilpisjärvi antenna beams. IRIS web.

The IRIS-Kilpisjärvi riometer data are available on-line upon request – also in real time. Applications should be forwarded via the IRIS link: http://www.dcs.lancs.ac.uk/iono/iris .

Imaging riometer data are processed to many different display formats. One type displays absorption in the area within the field-of-view of reliable beams (the black square in Fig 5.4.8.). With some interpolation the absorption intensities derived from the 49 discrete beams at any given time could be processed to provide a continuous 2-D map of absorption intensities with dimensions around 250 x 250 km. Such images can then be stacked to provide an overview of the time-history of absorption events.

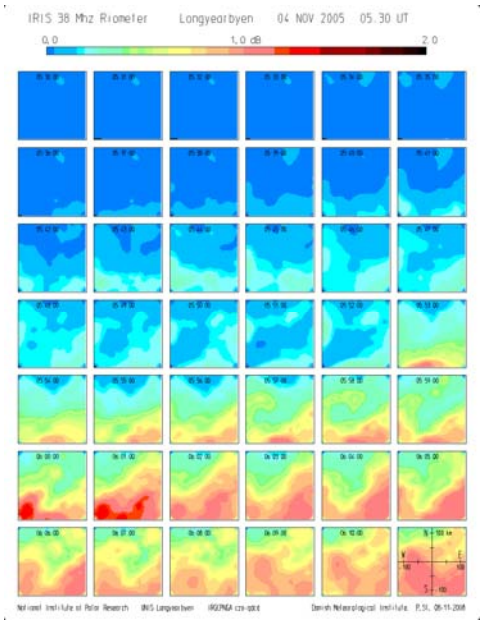

Figure 5.4.9. Sequence of absorption intensity maps. (Stauning, 2009)

An example is shown in Fig. 5.4.9. Here, a front of absorption (i.e. precipitating hard electrons) moves from SSE into and across the antenna field-of-view.

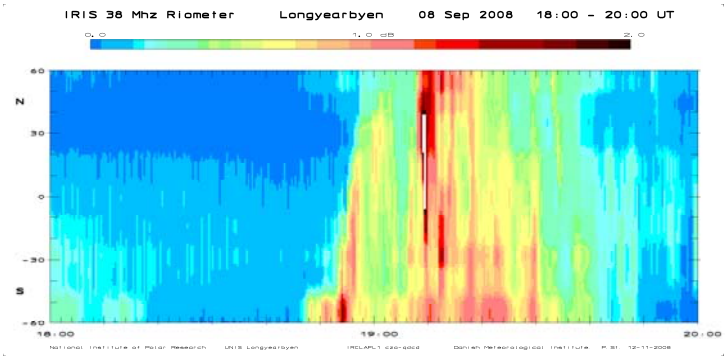

Figure 5.4.10. Absorption latitude-time intensity plot. (Stauning, 2009)

Such data can also be displayed in latitude-time diagrams as shown in Fig. 5.4.10. Here, the display extends 100 km north and south of the station. Each vertical strip in the diagram represents a N-S section of the instantaneous absorption image. The strips from a sequence of images are then stacked to provide a continuous time history of the latitudinal development. Note here that the region of enhanced absorption

starts in the south and then expands northward (poleward) ward to reach somewhat north of the field-of-view. Thereafter the absorption region retreats southward (equatorward). During this time several discrete intensifications (new onsets) occur where the enhancements is spread momentarily to provide vertical stripes within the "triangle" that encompassed the region of increased absorption intensities.

5.5. Coherent Scatter Radars.

Around 1960 it was realized that scatter reflections from irregularities in the ionosphere at frequencies much above those that could be reflected by normal refractive processes could hold important diagnostic information about the state and processes in the ionosphere (e.g., Bowles et al, 1963, Farley, 1963, Buneman, 1963). The examination of the spectrum of backscattered signals in experiments conducted near equator revealed Doppler shifts that to some extent could be explained by the line-of-sight component of electron and ion drifts in electric fields. However, when the electron drift velocity reached the speed of ion-acoustic waves then the apparent velocity would indicate saturation at values above the wave velocity level. At the same time the intensity of the backscattered signal would increase strongly.

It was also realized that in order to properly derive the drift velocities from observed line-of-sight values, a system of radars with overlapping beams would be required to convert the line-of-sight velocities into one velocity vector in the common volume. Furthermore, in order to receive a strong backscatter signal the direction of the radar beam should be such that the ray would intersect the ionospheric region perpendicular to the stationary magnetic field. The geometry of the signal path is illustrated in Fig. 5.5.1. The ionospheric irregularities that provide the backscatter of VHF signals are elongated in the direction of the magnetic field, which at high latitudes is nearly vertical. Hence some bending of the ray is required in particular for F-region backscatter or order to get the best aspect angle.

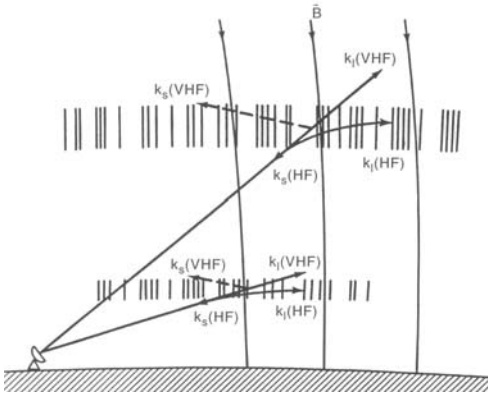

Figure 5.5.1. Scatter radar ray aspect angles. From Greenwald, 1996 [in Kohl et al. (1996), p.402]

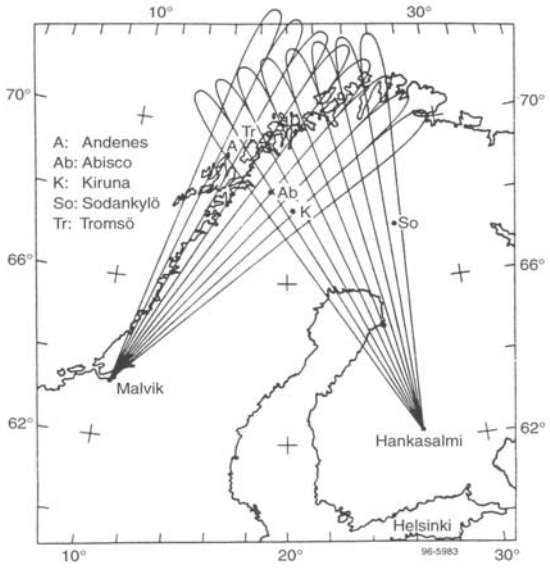

Figure 5.5.2. STARE dual radar beams. From Greenwald (1996), in Kohl et al., 1996, p.394.

The first radar system to be operated along these lines was the "Twin Auroral Radar Experiment", STARE, (e.g., Greenwald et al., 1978) followed by the "Sweden and Britain Radar Experiment", SABRE, (Nielsen et al., 1983). These systems have provided a wealth of insight both in the complicated plasma processes in the auroral ionosphere and also in its large-scale behaviour controlled by electric fields and currents coupled from the magnetosphere.

The STARE radar system consisted of a pair of bistatic very high frequency (VHF) radars located at Malvik in Norway and Hankasalmi in Finland, respectively, operated at frequencies in the 140-160 MHz band and having a common viewing area centred over northern Scandinavia. Each radar could transmit single/double-pulse signals into a 25° azimuth sector and receive backscattered signals on a 16-element antenna system connected to a 16-port Butler matrix. The central eight output ports of the Butler matrix were connected to eight parallel receivers. Thus, the backscattered signals could be sampled simultaneously from eight adjacent 3.6° azimuth sectors. The overlapping radar beams are illustrated on a map of Scandinavia in Fig. 5.5.2. The area

beneath the overlapping beams is approximately 400 x 400 km and includes two of the three EISCAT incoherent radar sites, Kiruna and Tromsø.

In brief, the examination of the spectra of the backscattered signals shall provide the width of the spectrum that is controlled by the plasma temperatures, and the displacement from the centre frequency (i.e., the Doppler shift), which measures the line-of-sight convection velocity of the irregularities that provide the backscattering. By using the pair of line-of-sight velocities the direction and magnitude of the ionospheric convection velocity can be derived over the field extended by the crossed radar beams. The convection, in turn, is mostly driven by the large-scale ionospheric electric field, **E**, projected from the magnetosphere. In the upper layers of the ionosphere the convection velocity, **V**, is:

$$\mathbf{V} = \mathbf{E} \times \mathbf{B} / B^2 \qquad (5.5.1)$$

where **B** is the stationary magnetic field vector. In the lower part of the ionosphere the convection is impeded by collisions between the ionized and neutral atmospheric constituents. In the lowest ionospheric layers the ions and electrons just drift with the neutral wind speed, **U**.

The electric field vectors derived from the plasma drift has been compared to values derived from rocket-borne in-situ measurements. An example is displayed in Fig. 5.5.3. Here the STARE electric field vectors have been plotted over a section of the field-of-view that also comprises the actual position of a double-probe electric field measurement on a sounding rocket. The electric field vector derived from the probe is added as a bar extending from the rocket position marked by a small circle. Most of the probe measurements are made in the region of electric field reversal in the so-called Harang discontinuity where the field magnitude is small and the direction uncertain but generally the agreement is quite good.

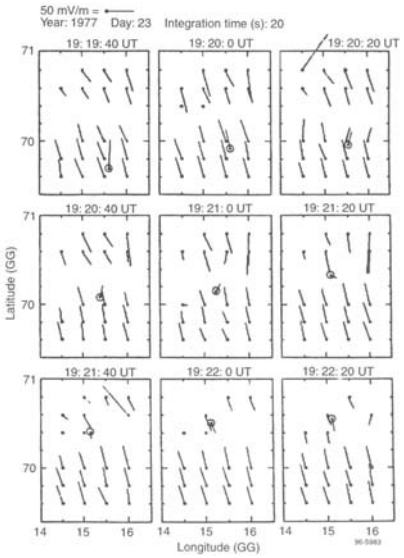

Figure 5.5.3. Comparison of STARE electric field with rocket-borne probe measurements. From Cahill et al., 1978 (in: Kohl et al., 1996, p.395)

STARE measurements have also been compared to EISCAT measurements of the plasma drift. For small values of the drift less than ~300 m/s corresponding to electric fields below 20 mV/m, the formation of irregularities is sparse and the backscattered signals are often not strong enough to be analyzed properly by the STARE radar. Above this threshold that corresponds to the ion-acoustic wave velocity the deduced STARE velocities do not rise as much as the velocities derived from EISCAT data but indicate saturation effects. Hence, the deduction of plasma drift velocities and electric fields from STARE radar-based velocities should be made with caution

In spite of these limitations, the interest for establishing a comprehensive monitoring of the ionospheric convection over the northern and southern polar region resulted in the establishing of a global Dual Auroral Radar Network, the SuperDARN, as an international radar network for studying the upper atmosphere and ionosphere. Presently, the SuperDARN system comprises eleven radars in the northern hemisphere and seven in the southern hemisphere.

The radars operate in the High Frequency (HF) bands between 8 and 22 MHz. In their standard operating mode, each radar scans through 16 beams of azimuthal separation 3.24°, with a total scan time of 1 min. Each beam is divided into 75 range gates of length 45 km, and so in each full scan the radars each cover 52° in azimuth and over 3000 km in range, an area of over 4×10^6 km². SuperDARN began in 1983, when the first radar installation was constructed in Labrador, Canada. Formal operation of SuperDARN as a global radar network started in 1995.

Like the STARE and SABRE radars, the SuperDARN radars measure the spectrum of Doppler velocities in signals scattered by plasma density irregularities in the ionosphere. However, in order to obtain the desired extended coverage the probing frequency was lowered such that the transmitted radar signals can be refracted in the F-region such as to meet the field-aligned scatter irregularities at right angle. The ray geometry for F-region scattering is sketched in Fig. 5.5.1.

An example of the data from a single radar beam is shown in Fig. 5.5.4. The equatorward moving enhancements in backscatter intensity are caused by atmospheric gravity waves. (From Bristow and Greenwald, 1995).

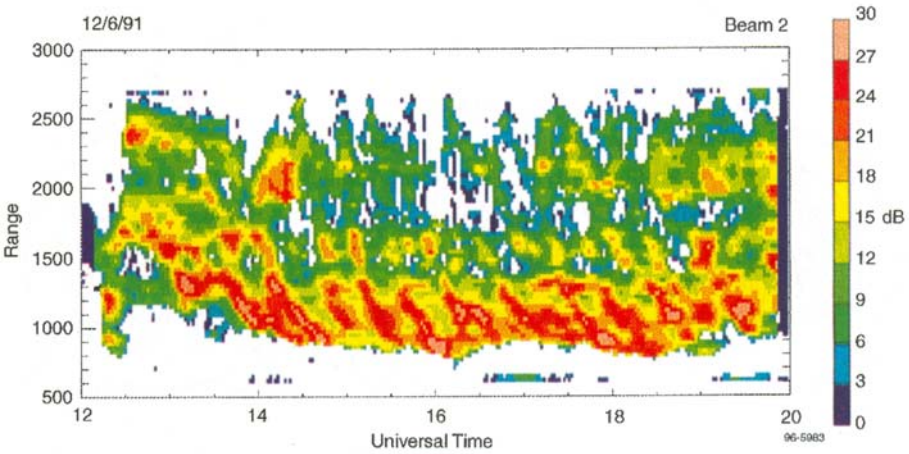

Figure 5.5.4. Example of a range-time diagram of signals from a single beam. (From Bristow and Greenwald, 1995. In Kohl et al., 1996, p.405)

From the received radio signals for a single radar, a number of parameters can be investigated, such as:

- line-of-sight neutral wind speeds in the mesosphere (~94 km)
- line-of-sight plasma drift speeds in the ionosphere (~100 km and 400 km altitude)
- speed, direction and wavelength of gravity waves in the ionosphere
- travelling ionospheric disturbances
- polar mesosphere summer echo occurrence (related to polar mesosphere/noctilucent clouds)
- meteor occurrence and altitude
- speed, direction and wavelength of ultra-low frequency magnetohydrodynamic waves
- space weather diagnostics (magnetic reconnection rate, magnetic field-aligned current)
- sea state

By combining such measurements from more than one radar, these phenomena may be measured across a wider range of scales, allowing estimation of:

- complete global convection in the ionosphere
- atmospheric tides and planetary waves

An example of global convection estimate is shown in Fig. 5.5.5. (from UK SuperDARN web site: http://ion.le.ac.uk/cutlass/superdarn.html).

The SuperDARN data are available in real time for associates of the SuperDARN community. Information on possible access to the data are provided on the SuperDARN web page: http://superdarn.jhuapl.edu

The photos in Fig. 5.5.6. display the most recent addition to the SuperDARN network provided by Virginia Tech. University.

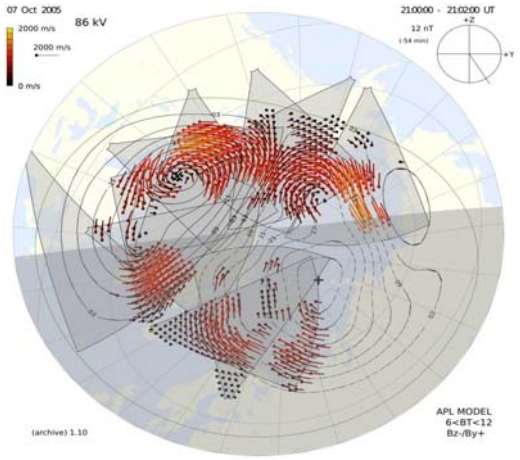

Figure 5.5.5. Estimate of polar convection patterns from SuperDARN measurements of drift velocities and contours of modelled potential distribution. (From UK SuperDARN web site)


Figure 5.5.6. Photos of Virginia Tech. SuperDARN installation. (From VT SuperDARN web site)

Links and further reading:

General info on ionosphere: http://www.swpc.noaa.gov/info/Iono.pdf
General info on radiowave propagation: http:// www.swpc.noaa.gov/info/Radio.pdf

Links to more information on Ionosondes and Digisondes:
How do you read the Digisonde Ionogram Plots: http://home.swbell.net/pjdyer/esiongrm.htm
Variables Explained - brief description of FoEs, FxEs, h'Es, etc.: http://ulcar.uml.edu/%7Eiag/CHARS.htm
NOAA NGDC Overview of Vertical Sounding: http://www.ngdc.noaa.gov/stp/IONO/ionogram.html
Basic Ionosonde Theory: http://www.wdc.rl.ac.uk/ionosondes/ionosonde_basics.html
Background to Ionospheric Sounding: http://ulcar.uml.edu/DPS.htm
Case Study of an Ionosonde Move: http://www.wdc.rl.ac.uk/ionosondes/contents.html

Online Ionosonde and Digisonde real-time data :
North America
HAARP - Gakona, AK: http://www.haarp.alaska.edu/haarp/data.html
College, AK: ftp://solar.sec.noaa.gov/pub/lists/iono_day/College_iono.txt
Haystack, MA: http://digisonde.haystack.edu/
Ionosonde, Tromsø Geophysical Observatory (TGO): http://geo.phys.uit.no/ionosonde/
Italy - Rome : http://dps-roma.ingrm.it/
United Kingdom - Fairford AFB ftp://solar.sec.noaa.gov/pub/lists/iono_day/Fairford_iono.txt

Riometer information and data:
Description: http://www.haarp.alaska.edu/haarp/Rio.htm
Riometer system: http://www.lajollasciences.com
Global riometer locations and data: http://www.dcs.lancs.ac.uk/iono/gloria
On-line data : http:// www.haarp.alaska.edu/haarp/data.htm
Imaging riometer: http://www.dcs.lancs.ac.uk/iono/iris

SuperDARN information and data:
SuperDARN Network at Johns Hopkins Applied Physics Laboratory http://superdarn.jhuapl.edu/
SuperDARN at the University of Alaska Geophysical Institute : http://superdarn.gi.alaska.edu

SuperDARN at Virginia Tech: http://www.space.vt.edu/superdarn
UK SuperDARN: http://ion.le.ac.uk/cutlass/superdarn.html
Super Dual Auroral Radar Network (SuperDARN real-time data (need registration and password):
http://superdarn.jhuapl.edu/archive/cnvmap.north.html
After registration: http://superdarn.jhuapl.edu/cgi-bin/validate.cgi

References:

Super Dual Auroral Radar Network (SuperDARN), Chisham et al., (2007), A decade of Super Dual Auroral Radar Network (SuperDARN): Scientific achievements, new techniques and future directions, Surveys of Geophysics, 28, 33-109, doi:10.1007/s10712-007-9017-8.

Detrick, D. L. and T. J. Rosenberg (1990), A phased-array radiowave imager for studies of cosmic noise absorption, Radio Science, 25, 325-338, 1990.

Hargreaves, J. K., Auroral absorption of HF radio waves in the ionosphere: a review of results from the first decade of riometry (1969), Proc. IEEE, 57, 1348-1373, 1969.

Little, C. G. and H. Leinbach (1959), The Riometer – a device for the continuous measurement of ionospheric absorption, Proc. IRE, vol. 47, p. 315.

Rawer, K. (ed.), Manual on ionospheric absorption measurements, World Data Center A for Solar-Terrestrial Physics, Report UAG-57, Boulder, 1976.

Stauning, P. (1996), High latitude D- and E-region investigations using imaging riometer observations. J. Atmos. Terr. Phys., 58, 765-783,

Stauning, P. (1996), Investigations of ionospheric radio wave absorption processes using imaging riometer techniques. J. Atmos. Terr. Phys., 58, 753-764.

Stauning, P. (1996), Ionospheric Investigations using Imaging-Riometer Observations, in: Review of Radio Science 1993-1996, ed.: W. R. Stone, Oxford University Press.

UAG Reports no. 23, "URSI Handbook on Ionogram Interpretation and Reduction"
and UAG report no. 50 "High Latitude Supplement" (NOAA, Boulder, CO)

Reference books:

Davies, K. (1990, 2008), Ionospheric Radio, First Edition: 1990, Peregrinus Ltd., Reprinted: 2008, The Institution of Engineering and Technology, London.

Hargreaves, J. K. (1992), The Solar-Terrestrial Environment, Cambridge University Press.

Kohl, H., R. Rüster, and K. Schlegel (eds.), Modern Ionospheric Science, European Geophysical Society, FRG 1996.

6. Concluding remarks.

When data from ground-based observations are used for Space Weather services, it is important to recall the properties of the observing instruments and the characteristics of their operation. Furthermore, it is important to observe the local conditions such as location in a geophysical sense (e.g., geomagnetic latitude), local time, season of the year etc.

A possible sequence in the scanning of data could be:

1. Check the Dst and Kp indices to see whether a magnetic storm is ongoing.

2. Check the AE and PC indices to see whether we are in a period of polar and auroral activity.

3. Look for possible solar flare effects (from enhanced solar UV- and X-ray radiation and radio noise) like crockets in magnetograms, excessive noise mixed with impulsive absorption events in riometer recordings. Such signatures at the dayside of the Earth and preferably at middle and low geomagnetic latitudes (away from the auroral as well as the equatorial electrojets and auroral absorption events) may signal the actual occurrence of a solar outburst.

4. Look for PCA events in riometer recordings and blackouts in ionosonde/digisonde recordings that could signal an intense solar proton event, which may start in the initial phase (within 15 min - 1 hour) of a solar outburst.

5. Look for signatures of Sudden Storm Commencement (SSC) in the horizontal component in mid-latitude magnetograms. SSC's are impulsive spikes that are strongest and positive at mid-day. They signal the arrival of the front of a CME cloud and may be some minutes ahead of the arrival of main bulk of CME ejecta.

6. Look around to real-time magnetograms from a number of on-line stations observing for disturbances and remembering to take into account their location and local time.

7. Check riometer recordings to observe for major auroral or polar cap absorption events.

8. Check real-time ionograms from on-line digisondes (dynasondes) to observe for irregularities in layer structures (e.g., layer heights, critical frequencies, scatter, black-out).

9. Check TEC maps to check for unusual features in the distribution or magnitude of the total electron content.

10. Hang-on to magnetograms from a selected on-line array (e.g. the Scandinavian magnetometers) to be alert to possible Space Weather developments.

--------- o ---------